Award #DE-LM0000479

Kamel Didan[1]

Christopher J. Jarchow[2]

Truman P. Combs[3]

Armando Barreto-Muñoz[4]

Unmanned Aerial System (UAS) Multispectral Data Calibration and Evaluation

Final Report

Best Practices for Collecting, Calibrating, and Processing Multispectral Imagery

[1]Professor, Biosystems Engineering, University of Arizona

Email: didan@arizona.edu

[2]Lead Scientist, RSI EnTech, LLC

Email: chris.jarchow@lm.doe.gov

[3]Ph.D Student, Biosystems Engineering, University of Arizona

Email: tpcombs@arizona.edu

[4]Associate Research Scientist, Biosystems Engineering, University of Arizona

Email: abarreto@arizona.edu

Project Dates[1]: May 21st, 2020-May 20th, 2023

March 2023

Final Report

Unmanned Aerial System (UAS) Multispectral Data Calibration and Evaluation

Sponsor: United States Department of Energy (DOE) Office of Legacy Management (LM), Applied Studies and Technology (AS&T) Program under grant #DE-LM0000479.

Project Dates[1]: May 21st, 2020-May 20th, 2023

March 2023

[1]The new dates reflect changes resulting from the COVID-19 Pandemic

Table of Contents

List of Figures

List of Tables

List of Abbreviations

AFT – Radiometric Calibration Image Collected Post-Flight
AGL – Above Ground Level
AOP – Airborne Observation Platform
BEF – Radiometric Calibration Image Collected Pre-Flight
BRDF – Bidirectional Reflectance Distribution Function
DN – Digital Number
DOE – Department of Energy
EM – Electromagnetic Spectrum
EVI2 – Two-band Enhanced Vegetation Index
FOV – Field-of-view
GCP – Ground Control Point
GRP8 – Group-8 Radiometric Calibration Panel
IC – Independent Checkpoint
LiDAR – Light Detection and Ranging
LM – Office of Legacy Management
MAPR – MAPIR Radiometric Calibration Panel
MS – Multispectral
NDVI – Normalized Difference Vegetation Index
NEON – National Ecological Observatory Network
NIR – Near-infrared
NIT – Nearest-in-time
P4M – DJI Phantom 4 Multispectral
P4P – DJI Phantom 4 Pro
RGB – Red-Green-Blue
RMSE – Root Mean Square Error
$RMSE_{BGRN}$ – Composite RMSE calculated from Blue, Green, Red, and NIR
$RMSE_{Blue}$ – RMSE calculated from the Blue Reflectance Image
$RMSE_{EVI2}$ – RMSE calculated from the EVI2 Image
$RMSE_{Green}$ – RMSE calculated from the Green Reflectance Image
$RMSE_{NDVI}$ – RMSE calculated from the NDVI Image
$RMSE_{NIR}$ – RMSE calculated from the NIR Reflectance Image
$RMSE_{Red}$ – RMSE calculated from the Red Reflectance Image

$RMSE_X$ – RMSE calculated from the GCP Analysis for the geospatial X dimension
$RMSE_Y$ – RMSE calculated from the GCP Analysis for the geospatial Y dimension
$RMSE_Z$ – RMSE calculated from the GCP Analysis for the geospatial Z dimension
ROC – Relative Optical Center
ROI – Region of Interest
RSR – Relative Spectral Response
RTK – Real-time Kinematic
SNR – Signal-to-noise Ratio
SRER – Santa Rita Experimental Range
SSE – Sum of Squared Errors
ToD – Time of Day
UAS – Unmanned Aerial System
UAV – Unmanned Aerial Vehicle

1. Executive Summary

This document presents the findings of a project conducted by the University of Arizona Vegetation Index & Phenology Laboratory on behalf of the U.S. Department of Energy Office of Legacy Management (LM) that compared unmanned aerial system (UAS) multispectral (MS) data to a high-fidelity hyperspectral reference to develop a suite of best practices for the collection, radiometric calibration, and processing of UAS MS imagery. We evaluated a series of factors that contributed to error propagation throughout the data collection and processing workflow, which we investigated through a series of precisely designed UAS missions conducted concurrently with the National Ecological Observatory Network (NEON) Airborne Observation Platform (AOP) hyperspectral observation flight mission over a region of rangeland with a wide array of vegetation densities (i.e., a proxy for landcover conditions that may be observed at LM sites). We considered timing of MS image collection, camera view angle, flight altitude, timing of radiometric calibration, ground control (spatial accuracy), and error associated with vegetation density. Manufacturer-provided MS image processing procedures (consistent with industry guidelines for commercial-grade UAS technology) were evaluated stepwise for impacts on the error relative to fully corrected UAS MS imagery, focusing on the following procedures: dark current correction, vignette correction, radiance (W/m^2-steradian) calculation, surface reflectance (unitless: 0 – 1.0) calculation, and lens distortion correction. We show that MS collection, radiometric calibration, and processing procedures all impact UAS MS data accuracy relative to a reference, but that error propagation can be mitigated with careful mission planning and implementation of optimized procedures. Section 5 of the report provides a summary of procedural recommendations supported by our findings and peer-reviewed literature.

2. Introduction

Unmanned aerial systems (UASs) present an unprecedented opportunity for surveying landscapes at high spatial resolutions. UASs consist of the unmanned aerial vehicle (UAV), operator, and all associated equipment that support flight operation. With advances in miniature cameras and sensor technology, demand for drone use in land monitoring and management is expected to grow. Currently, UAV-mounted multispectral (MS) cameras (i.e., imaging devices that collect information in one or more spectral bands in the visible and near-infrared regions of the electromagnetic spectrum (EM)) lack robust standard operating procedures for collecting, calibrating, and processing these data across diverse research applications and environmental conditions. Deriving accurate surface reflectance data, the basis for most value-added products from MS cameras, remains a challenge due to variable UAS viewing geometry, landcover conditions and spatiotemporal change, radiometric calibration, image correction procedures inherent to sensor optics, and UAV performance. To help characterize these factors, we evaluated the following, looking to develop a set of best practices and operating procedures for the collection and processing of MS data:

- Optimal time of day (ToD) for data collection
- Optimal flight altitude
- Optimal viewing geometry
- Best practices for radiometric calibration

- Sensor performance across varying vegetation densities
- Necessary data processing steps and procedures

3. Methods

3.1. Study Site

The unmanned flights and associated fieldwork were coordinated with the National Ecological Observatory Network's Airborne Observation Platform (NEON AOP; hereafter referred to as AOP) annual summer data collection campaign at the Santa Rita Experimental Range (SRER) (Figure 1a). The SRER is a 21,000-hectare field station located south of Tucson, AZ which is jointly managed by the University of Arizona and the U.S. Department of Agriculture. The SRER represents one of NEON's 81 field sites in 20 ecoclimatic regions located across the United States and Puerto Rico. The rangeland is bordered to the south by the Santa Rita Mountains (Coronado National Forest). Its geology and soils vary across a 500-m elevation gradient and several vegetation types. The SRER predominantly consists of desert rangeland characterized by arid and semi-arid vegetation with localized zones of verdant riparian vegetation. This range of vegetative cover, spanning from bare soil to dense vegetation (Figure 1b), is representative of the full range of spectral conditions (i.e., dynamic range of vegetative cover) expected at Department of Energy (DOE) Office of Legacy Management (LM) sites across the U.S. AOP flights at the SRER are generally conducted when cloud cover is ≤10% and vegetation is ≥90% of maximum greenness.

a)

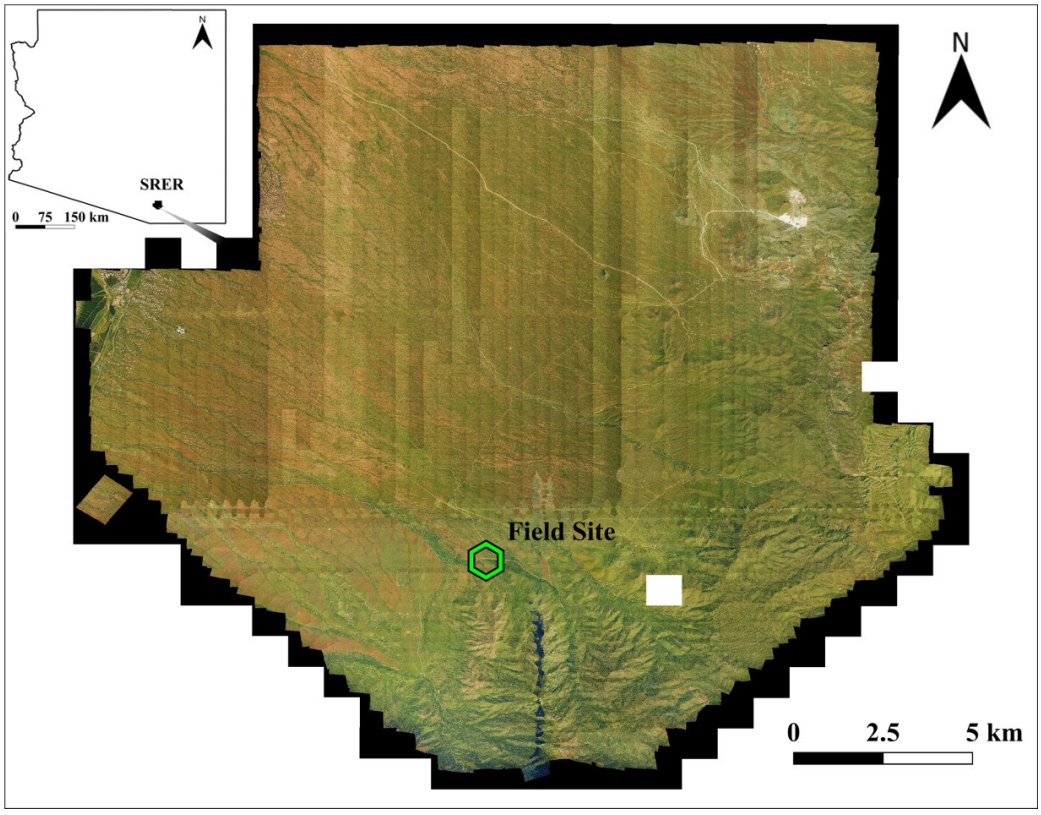

b)

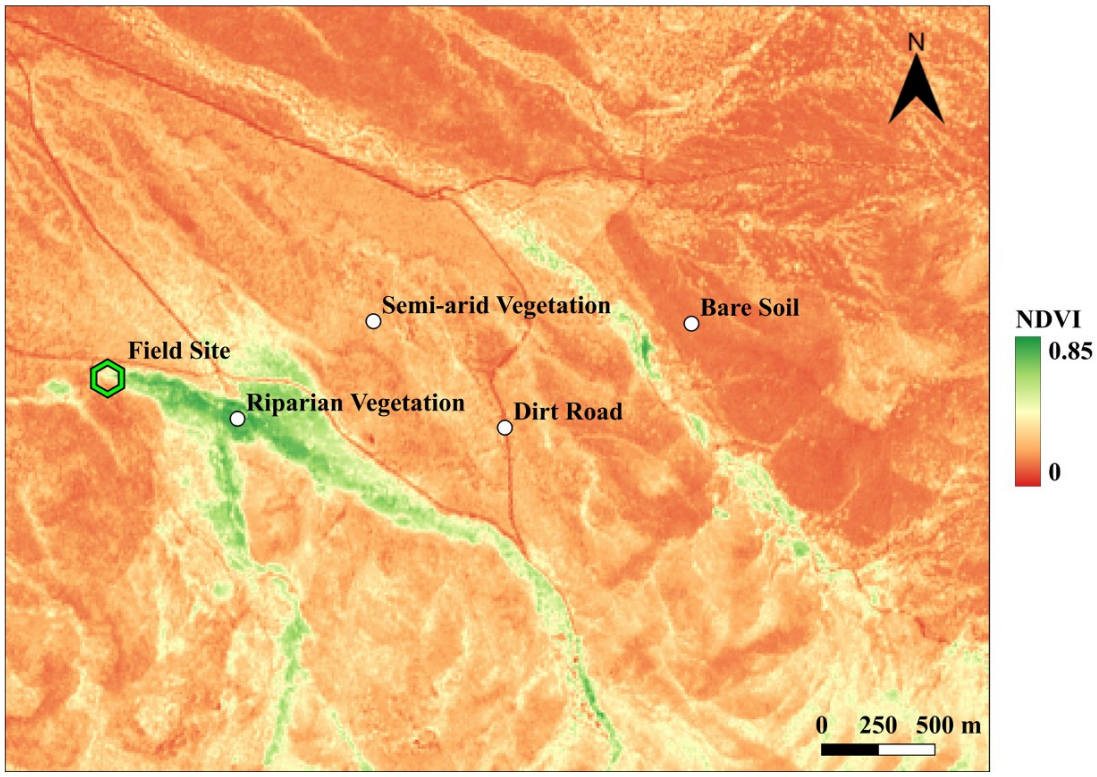

Figure 1. (a) Natural color imagery collected by the AOP over the SRER. Orthorectified image mosaics are distributed by NEON in 1 km tiles. (b) Normalized difference vegetation index (NDVI) is a measure of plant greenness, with landcover values typically ranging from 0 (bare soil) to 1 (densely vegetated). Our SRER field site has the full range of these conditions over a short distance, making it an ideal proxy for sites managed by DOE LM.

3.2. Equipment

3.2.1. UAS Platform

Most modern UAV platforms and MS cameras are sold as separate units, often by different manufacturers, with options for integration. To minimize UAS-camera incompatibilities, integration challenges and potential errors in data collection, we used a DJI Phantom 4 Multispectral (P4M) platform (Figure 2a) which has a gimballed MS camera system consisting of six 1/2.9" CMOS sensors corresponding to blue (434 – 466 nm), green (544 – 576 nm), red (634 – 666 nm), red edge (714 – 746 nm), near-infrared (NIR; 814 – 866 nm), and natural-color, red-green-blue (RGB) imagery (Figure 2b). The red edge band corresponds to a region of the EM spectrum that captures the sudden change from high absorption of photosynthetically active radiation (visible light) to highly reflected NIR; however, it presents limited quantitative value and is not typically used in computing common vegetation indices (VIs; standardized remote sensing measures used in long-term vegetation monitoring) like the normalized difference vegetation index (NDVI). Therefore, red edge data were omitted from analysis. The aircraft also offers the operator full control over the gimbal pitch, allowing for precise view-angle manipulation ranging from nadir (i.e., camera pointed directly below the aircraft) to 90° off-nadir (i.e., camera pointed directly

ahead). Additionally, the P4M platform provides a rich set of tools for mission planning and automated execution, in-flight control, telemetry, video feedback, and nearly 30 minutes of flight time per battery.

a)

b)

Figure 2. (a) The DJI P4M is a unique platform that provides (b) an integrated MS gimballed camera with real-time kinematic (RTK) geo-positioning capabilities (https://www.dji.com/p4-multispectral).

3.2.2. Reference Platform: NEON AOP

The AOP consists of a fixed-wing aircraft flying at a nominal altitude of 1 km above ground level (AGL) to collect light detection an ranging (LiDAR) data with a spatial resolution of 1 m/pixel, hyperspectral data with a spatial resolution of 1 m/pixel, and true-color RGB imagery at 10 cm/pixel (Figure 3a, 3b; Gallery, 2022). The AOP imaging spectrometer (i.e., hyperspectral sensor) uses a pushbroom scanning mechanism with a 34° field-of-view (FOV). The pushbroom scanner, also known as linear array sensor, uses detectors arranged perpendicular to the flight path to collect incident light without the need for any mechanical parts in the imaging system, which minimizes pixel deformation. Spectral measurements are collected near-continuously with a 5-nm full-width half-max bandwidth spanning from 380 to 2500 nm across the EM spectrum, resulting in 426 unique bands. These specifications, in combination with the AOP's rigorous sensor and data calibration procedures (Shrestha et al., 2020), provided a robust, validation quality reference dataset for this project.

a)

b)

Figure 3. (a) Infographic depicting the various datatypes collected by the AOP (Credit: NEON). (b) The AOP flying over the SRER field site during the summer 2021 data collection campaign (Credit: Christopher Jarchow).

3.2.3. Radiometric Calibration Panels

Optimal radiometric calibration procedures were evaluated using reference panels (i.e., a specially coated surface with precisely known and traceable reflectance values) from Group 8 Technology, Inc. (GRP8; Figure 4a) and MAPIR, Inc. (MAPR; Figure 4b). Both panels consisted of four sub-panels, each corresponding to different grayscale levels with fully traceable reflectance values for each wavelength. MAPR provides reflectance data for its panel at each wavelength (nm) between 350 and 1100 nm, while GRP8 reports nm-level reflectance from 300 to 2500 nm. The MAPR panel contains sub-panels corresponding to 2%, 21%, 27% and 83% reflectance, while the GRP8 panel contains sub-panels corresponding to 12%, 36%, 56% and 84% reflectance. We evaluated the following subset of sub-panels in our analyses, separately: 21% (MAPR), 27% (MAPR), 36% (GRP8), and 56% (GRP8). Accurate radiometric calibration of MS sensors involves placing the reference panel in an area with direct sun exposure and using the MS camera to image one or more reference sub-panels, following guidance provided by Yoon and Kacker (2015). This creates a precise record of the illumination conditions (incident light) which is used during image processing to compensate for any changes in solar radiation reaching the imaged scene. This process accounts for solar geometry (ToD and latitude) and atmospheric contaminants (gases, aerosols, dust, water vapor) that may reduce the amount of incident light. It should be noted that radiometric calibration cannot overcome the effects of cloud cover (e.g., shading the scene), in which case surveys should be rescheduled to a time with cloud-free conditions. Radiometric calibration panels are Lambertian surfaces with no directional preference to the acquisition geometry, ensuring a stable, high-fidelity response to incident light. These high accuracy reference panels have known reflectance values over a wide range of the visible and NIR wavelengths, thus allowing for the accurate computation of total incident light. The MS camera records metadata required to compute the radiance from each pixel in the scene, which is converted into surface reflectance after dividing by light incident on the surface (Wang, 2021). The process for converting radiance to surface reflectance using the radiometric calibration panel is described in Section 3.4.4.

We collected radiometric calibration images over the MAPR panel by holding the aircraft approximately 1 m AGL and directly above the panel with the camera pointing nadir (Figure 4b). MAPR radiometric calibration images were collected immediately before (BEF) and after (AFT) each UAV mission, generally within 2 minutes. We also evaluated the accuracy of using the radiometric calibration image collected nearest-in-time (NIT) to each MS image requiring correction. For example, for a UAV flight lasting 15 minutes, the MAPR radiometric calibration image collected immediately following the completed mission would be used to calibrate any MS imagery collected after 7 minutes and 30 seconds of flight time, while the first radiometric calibration image would be used to calibrate all MS imagery collected in the first 7 minutes and 30 seconds.

In-flight GRP8 radiometric calibration data were extracted from MS imagery (i.e., separate radiometric calibration images of the GRP8 panel were not collected prior to or following each mission) due to the GRP8 panel's placement in the field and lack of accessibility (Figure 4a). For those viewing altitudes evaluated in this project (Section 3.3.1), in-flight imaging of the GRP8 panel exhibited extreme saturation in the blue, green, and red bands across all sub-panels with reflectance >12%, likely a result of the flight altitude and brightness at the time of image

acquisition. The darkest (12%) sub-panel could still be distinguished from other sub-panels for the red and green bands, but sub-panels were not distinguishable in the blue band. No sub-panels were saturated in the NIR, which allowed our team to derive the ratio between the 12% sub-panel and the remaining sub-panels for the NIR band. Using these NIR derived ratios, we estimated the unsaturated radiometric correction coefficients (described in Section 3.4.4) corresponding to each saturated sub-panel for blue, green, and red bands. We used saturation-adjusted radiometric correction data for GRP8's 36% and 56% sub-panels in subsequent analyses, while the MAPR reflectance panel (21% and 27%) did not require any adjustment prior to use in radiometric calibration. Similar to the MAPR technique, which considers a NIT radiometric calibration approach in addition to BEF and AFT radiometric calibration procedures, we selected a subset of MS images collected at 40 m AGL (i.e., lowest flight altitude considered in our analyses) and multiple camera view angles over the duration of the UAV missions for extracting radiometric calibration information from the field-deployed GRP8 panel.

Figure 4. (a) GRP8 and (b) MAPR radiometric calibration panels, each containing multiple grayscale sub-panels corresponding to known traceable reflectance values. The GRP8 panel was located within the UAV's flight path for all UAS missions, while the MAPR panel was imaged with the UAV in-hand at a short distance above the ground before and after each flight.

3.2.4. Ground Control

We evenly distributed 22 ground control points (GCPs; used for georeferencing the UAS imagery) and 23 independent checkpoints (ICs; used to independently quantify spatial error in georeferenced maps) in an alternating, rectangular framework within the study area to assess spatial accuracy of the UAS-derived maps produced using different configurations of GCPs (Figure 5a). We designed the GCP and IC (jointly referred to hereafter as targets) count and spacing based on a mid-range altitude of 75 m AGL, P4M field of view, and an additional setback from these viewing parameters to ensure the targets remained visible during the UAV overpass. Final target locations were adjusted from the theoretical distribution in some cases due to local topography and canopy cover encountered at the site (Figure 5b). We secured targets with metal stakes and surveyed their locations on September 29, 2021, following the completion of all UAS missions. Target positions were recorded between 2:19 PM and 3:51 PM local time using a DJI D-RTK 2 high-precision GNSS mobile base station placed on an elevated, nearby hill (31.77098° N, 110.86909° W; Figure 5c). The location of the base station was updated (prior to target surveying) via the nearby Amado, AZ Continuously Operating Reference Station (geodesy.noaa.gov/CORS/). The targets were

surveyed using the DJI GS Pro flight planning application, which reports positioning status as Float (meter level accuracy), Single (decimeter level accuracy) or Fixed (centimeter level accuracy). DJI advises users to wait until Fixed status has been acquired for mapping projects but does not specify a length of time required for signal stabilization. For all targets, we confirmed Fixed status prior to positional recording, which typically occurred within 30 seconds.

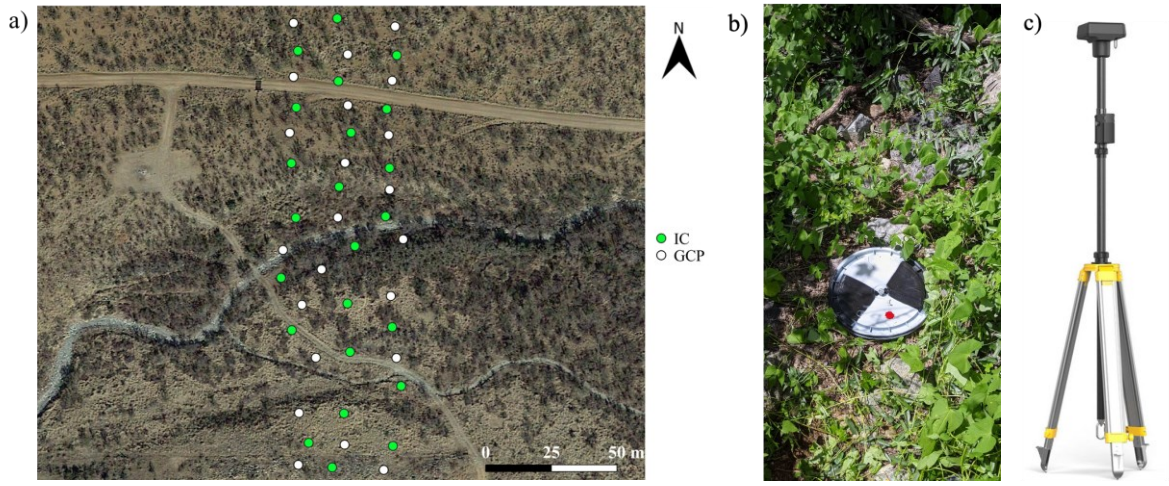

Figure 5. (a) Adjusted, final locations of the GCPs (white) and ICs (green). (b) High-contrast targets used for GCPs and ICs. (c) DJI D-RTK 2 high-precision GNSS mobile base station.

3.3. Mission Designs

We designed both plot and transect UAS missions to address most research objectives. We used a circularly scanning mission conducted over the area of the plot mission (hereafter referred to as a concentric mission) to investigate the effects of viewing geometry (bidirectional reflectance distribution function (BRDF)) on data accuracy. BRDF defines how radiance is reflected from a surface in a particular direction relative to the total incident light received by the same surface (Di Girolamo, 2003), which depends on the UAS viewing geometry relative to solar azimuth and zenith angles. The concentric mission followed the principles of a BRDF measurement with a goniometer (an instrument designed to sample observations across all azimuth and zenith angles).

UAS MS data collection missions aimed at evaluating view angle, flight altitude, collection timing, radiometric calibration, performance across varying vegetation densities, and image processing procedures were conducted on September 7, 2021 – the same day of the AOP's data collection (which occurred at ~10:30 AM) – over our site. Solar azimuth and elevation angles for September 7, 2021, are presented in Figure 6a and 6b, respectively. We collected ancillary UAS data on September 3 and September 29, 2021, using a single-grid type mission (i.e., a UAS mission type common to many mapping applications with parallel flightlines, the density of which reflects a desired level of overlap between adjacent images) to support our georeferencing analysis (See Section 4.5).

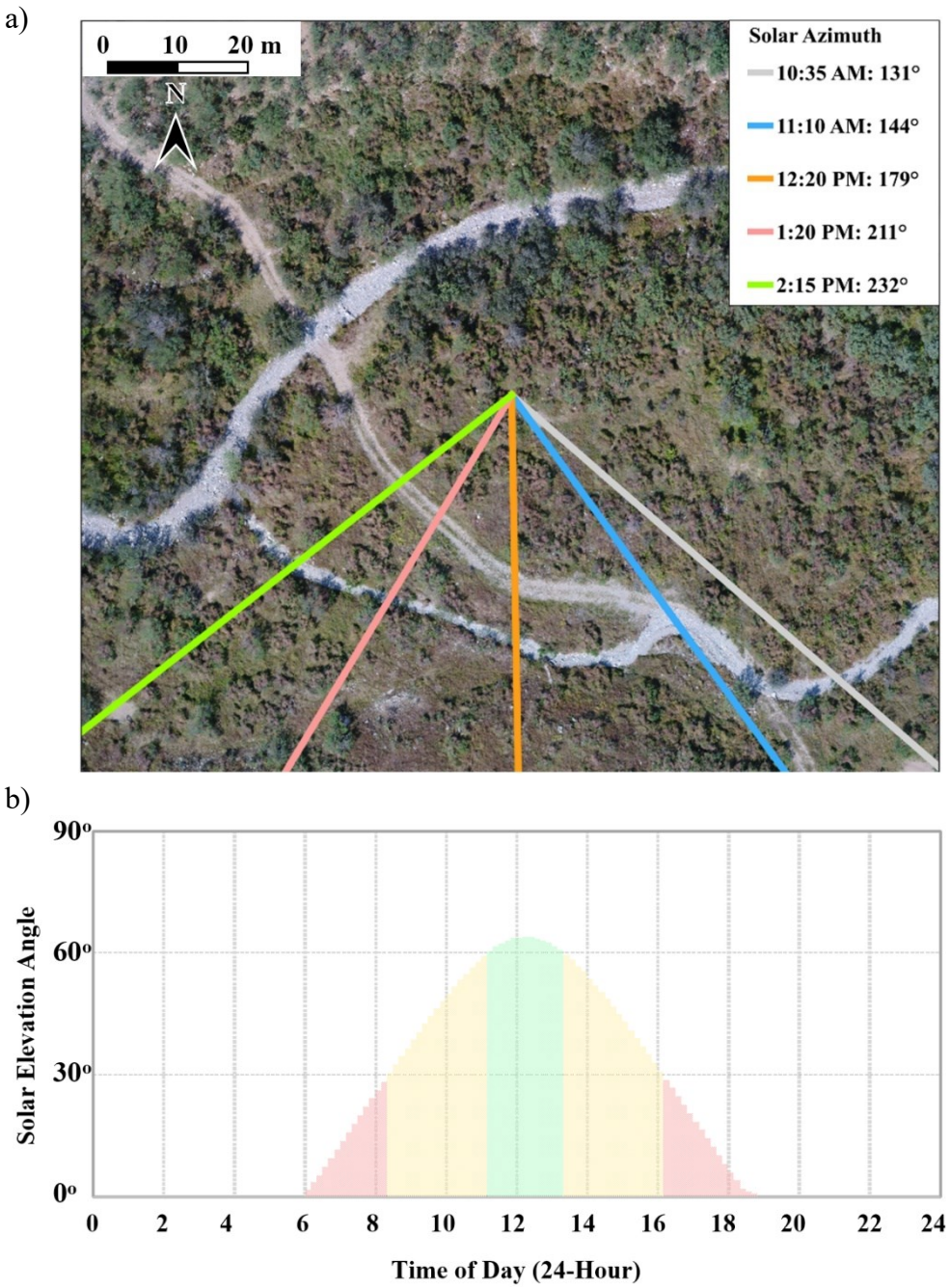

Figure 6. (a) Approximate solar azimuth angle for each of the plot missions (see Section 3.3.1) as provided by NOAA and (b) solar elevation angle versus time for the date of concurrent UAS-AOP surveys (September 7, 2021) as computed by the DJI GS Pro flight planning application. The application recommended UAS operations occur between approximately 8:20 AM and 4:10 PM local time (yellow and green regions). UAS operations outside this window of time (red regions) were not recommended since the solar elevation angle was too low.

The plot, transect, and concentric missions were designed in UgCS (SPH Engineering, 2023), a commercial flight planning tool. To determine the mission waypoint (i.e., 3-dimensional spatial coordinate locations that guide the aircraft movements), we developed a trigonometric model that

estimated the aircraft waypoints required to capture the desired camera observations based on combinations of gimbal pitch, flight altitude, and UAV heading. The computed waypoints were uploaded to UgCS to visualize, confirm, and execute the final missions.

3.3.1. Plot Mission

The plot mission addressed the following research objectives:

- Optimal ToD for MS data collection
- Optimal flight altitude
- Optimal viewing geometry
- Best practices for radiometric calibration
- Impacts of MS data processing steps on corrected surface reflectance

Nadir viewing is conventionally preferred for collecting hyperspectral and MS data. However, collecting nadir imagery is not always practical due to flight mission planning, sensor optical constraints, and observation altitude. Nevertheless, the effect of off-nadir viewing on UAS MS imagery needs better characterization to inform mission planning. The impact of flight altitude on image accuracy with respect to a reference for low-altitude UAS operations is similarly not well understood since canopy features and shadow visibility may co-vary with altitude. Collection of radiometric calibration reference data, which is necessary for converting between radiance and surface reflectance, is presumed largely time-dependent due to the highly dynamic nature of solar and cloud-cover conditions. Additional atmospheric influences are assumed negligible at typical UAV flight altitudes. To disentangle the impacts of view angle (i.e., UAV gimbal pitch), flight altitude, and radiometric calibration on data accuracy, our systematic investigation focused on a subset of discretized view angles, flight altitudes, and radiometric calibration procedures. Finally, these data collection procedures were evaluated over varying vegetative densities (a proxy for sensor dynamic range) to capture the full range of cover conditions (i.e., bare soil, moderately vegetated, and fully vegetated) as determined by NDVI (ranging from approximately 0 to 1 for landcover types explored here). NDVI values below 0 were not considered as they correspond to water and snow.

Flight altitudes were restricted to between 40 m (minimum safe altitude in complex terrain) and 100 m (approaching the Federal Aviation Administration upper limit of 400 ft in uncontrolled airspace) AGL and evaluated in 20-m increments. It should be noted that increasingly higher spatial resolutions resulting from low altitude flights (<40 m AGL) are likely to introduce large levels of noise in the MS data that result from canopy structural changes caused by wind and from viewing different parts of the canopy profile.

UAV waypoints were oriented linearly west-east to standardize the solar azimuth angle relative to the UAV heading. We restricted viewing angles between 30° (W) (i.e., 30° gimbal pitch with a due west heading of 270°) and 30° (E) (i.e., 30° gimbal pitch with a due east heading of 90°) off-nadir and captured images in 10° increments, a range that should cover most of the view angles encountered in UAS remote sensing (Figure 7a). Angles >30° would likely introduce considerable

BRDF error, as a larger proportion of the canopy profile is captured by the sensor. We note here that these restrictions and viewing conditions are designed to support repeatable and accurate data collection specific to MS imaging, whereas RGB imaging follows other practices in which large view angles and lower altitude flights are more desirable (e.g., to generate a point cloud using structure-from-motion photogrammetry).

Commonly, UAS flight planning calls for the aircraft to stop at each waypoint before taking a photograph. This stop-and-shoot technique resulted in excessive battery consumption, often requiring multiple battery changes per mission, which imposed limits on the number of waypoints we could include in the mission design process. To increase efficiency, we eliminated all intermediate stops along each view angle and programmed the camera to shoot at prescribed intervals between the lowest and highest altitude for each view angle. The technique allowed for the camera view angle to remain fixed on a particular area as the UAV flew between 40 and 100 m AGL, before proceeding to the next prescribed view angle. This approach ensures that the imaging altitudes stay uniform across view angles and the number of photographs collected for each view angle are equal. The resulting dataset included 7 view angles collected in 10° increments between 30° (W) and 30° (E) (i.e., 30° (W), 20° (W), 10° (W), 0° (E), 10° (E), 20° (E), 30° (E)) and ranging between 40 m and 100 m AGL, for a total of 28 imaged locations (Figure 7b). Plot missions were conducted at five, approximately 1-hour time steps (ranging from 35 to 70 minutes apart) between approximately 10:00 AM and 2:00 PM local time to address the impact of ToD (i.e., solar elevation and azimuth angles; Figure 6a, 6b) on data accuracy, which resulted in 112 unique views of the plot scene (inclusive of all MS bands).

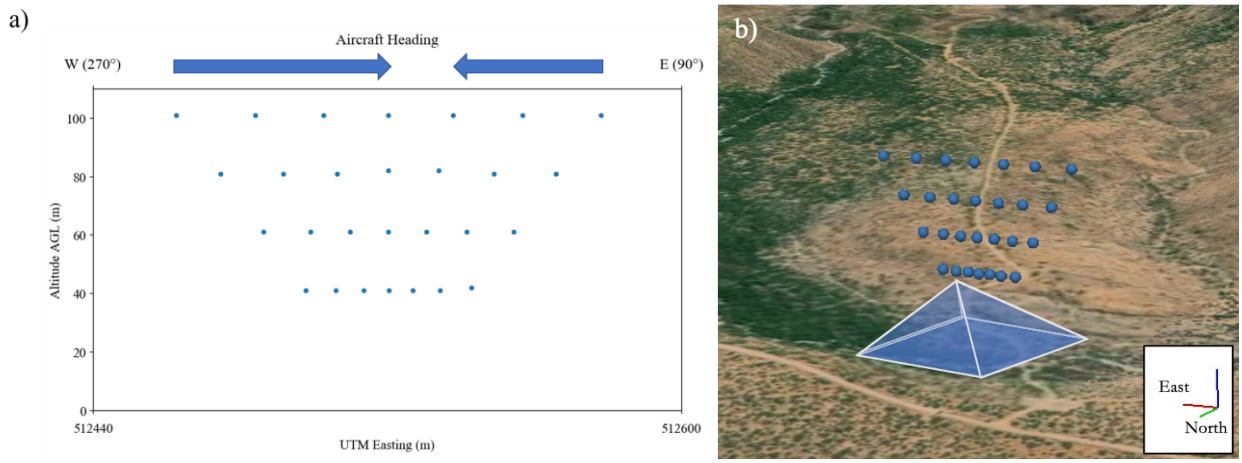

Figure 7. (a) 2-dimensional illustration of waypoints used during the plot mission. Images were collected at each waypoint by manipulating UAV altitude, heading, and view angle of the MS camera. (b) 3-dimensional illustration of the 28 aircraft positions where the UAV collected images during the plot mission.

3.3.2. Transect Mission

The transect mission allowed us primarily to assess performance across the range of vegetative cover expected across DOE LM sites, ranging from bare soil to densely vegetated. We deliberately constrained the flight parameters to 75 m AGL (a mid-range altitude) and nadir viewing to ensure adequate viewing of the GCPs and ICs (Figure 5a, 8; See Section 3.2.4). We conducted the mission

at approximately 12:00 PM local time to minimize shadows related to solar azimuth and elevation angles (Figure 6a, 6b).

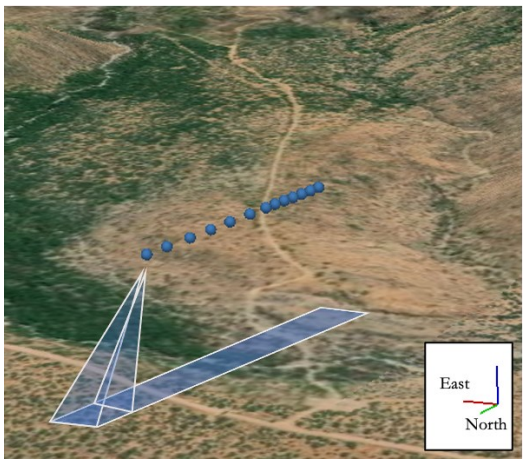

Figure 8. Illustration of the flight line and waypoints used for image acquisition during the transect mission.

3.3.3. Concentric Mission

One concentric mission, following the principles of a BRDF measurement with a goniometer (Figure 9a), was conducted using the plot design's trigonometric calculations to determine the waypoints for positioning the UAV relative to the plot's centroid, such that a particular combination of aircraft heading (i.e., yaw), gimbal pitch, and altitude parameters would result in the camera maintaining a full view of the plot footprint (Figure 9b). Rather than operating strictly from west to east as in the plot mission, the concentric mission maintained a view of the plot from a prescribed distance, altitude (between 70 and 75 m AGL, depending on the underlying topography), and view angle (10° and 30° were selected as representative of off-nadir viewing) while deliberately changing the heading of the aircraft by 20° steps (i.e., 18 images required to completely encircle the area). The result was a 360° near-continuous view of the plot from different angles.

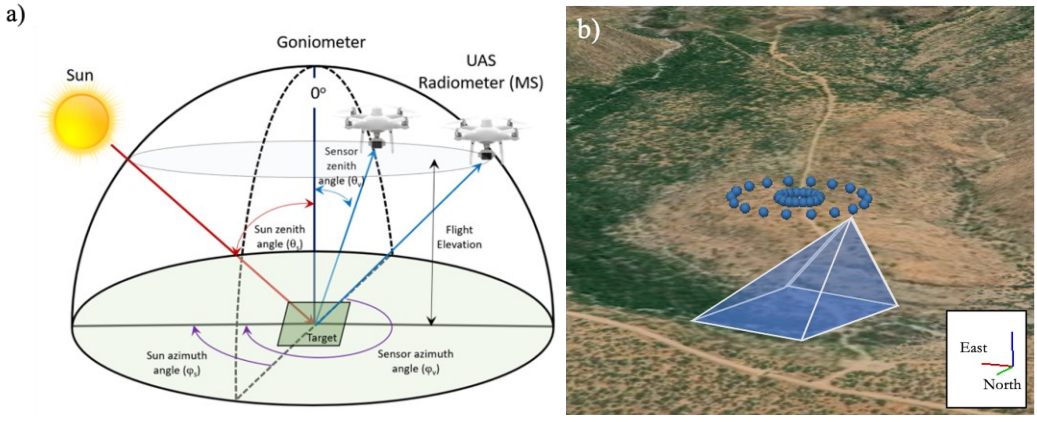

Figure 9. (a) A goniometer-type design was used for the concentric mission. (b) Illustration of a concentric mission, with multiple view angles captured at a single altitude.

3.4. Multispectral Data Processing Workflow

The data processing pipeline adopted for the UAS MS imagery follows standard processing and manufacturer guidance on correcting and converting tagged image file format (.TIFF) images from raw digital numbers (DN) to surface reflectance. This approach requires the use of a radiometric calibration reference (panel) for the derivation of surface reflectance. The process also relies on the OpenCV Python library (a powerful library with extensive image processing capabilities) to perform lens distortion, vignette, and band alignment corrections, all of which are standard image processing procedures performed by commercially available photogrammetric software. We did not assess the impact of band alignment given its extrinsic nature relative to intrinsic distortions requiring correction (discussed below). Figure 10 shows the workflow adopted for converting raw DN images to surface reflectance.

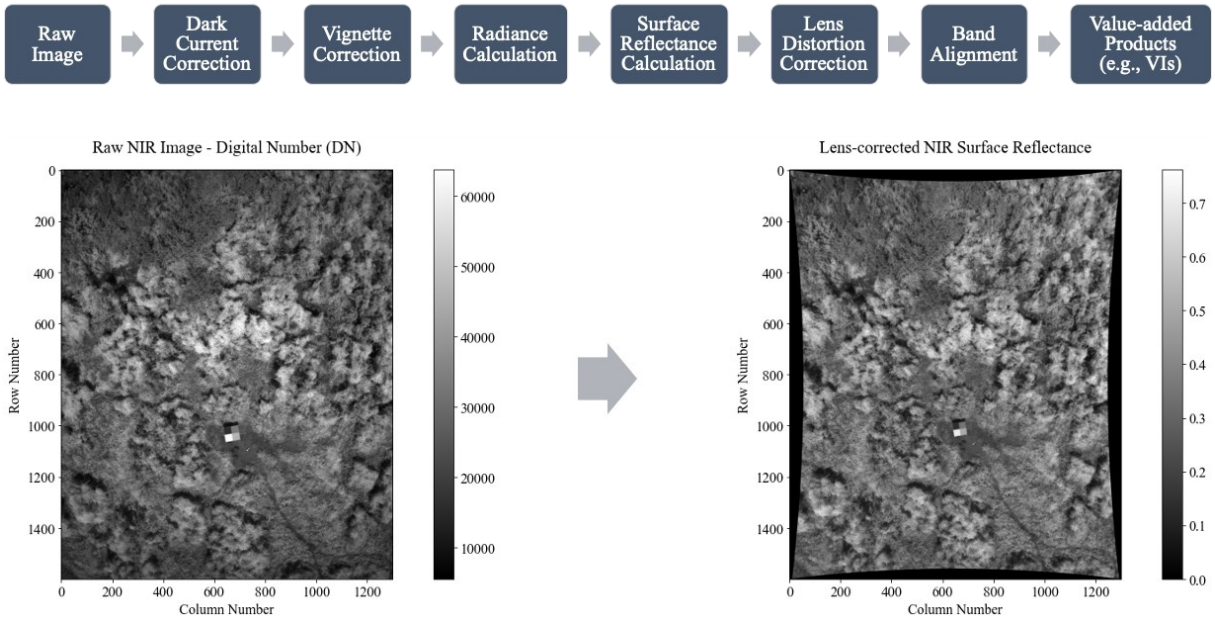

Figure 10. Full workflow required to convert raw DNs to surface reflectance.

DJI outlined a series of required corrections steps for the images collected by their P4M platform (DJI, 2020). These procedures, while consisting mostly of standard MS image processing steps, require specific parameters related to the electro-optical properties of the MS camera. These camera-specific parameters were provided as image metadata (i.e., tags) appended to each image. All relevant metadata needed during image correction was extracted using ExifTool, an open-access, Perl-based command line utility for manipulating image metadata (Harvey, 2023).

Additionally, we used Pix4Dmapper, a widely used, commercial photogrammetric software to process the 15 images collected during P4M MS transect mission from September 7, 2021 (date of concurrent flight with the AOP), P4M MS single-grid mission with high forward and side overlap conducted over the transect region on September 3, 2021, and a DJI Phantom 4 Pro (20-megapixel RGB) single-grid mission dataset collected over the transect region on September 29, 2021. This end-to-end image processing program provided additional capabilities to address the

research objectives, especially sensor and MS data performance over varying vegetation densities, the effect of the georeferencing process on absolute spatial accuracy, and the impact of radiometric calibration timing on relative radiometric accuracy.

3.4.1. Dark Current Correction

Per DJI, the dark current correction factor for the P4M is 4096 (DN). This value is used to offset the raw data and correct temperature-dependent and camera startup noise, a false-positive value registered by the detectors' elements of the camera when no light exists. The noise reduction coefficient is often derived from an average pixel value over a closed shutter acquisition or provided by the manufacturer as an image tag (as was the case here).

3.4.2. Vignette Correction

The vignette phenomenon refers to light fall-off across the frame relative to the center of the frame and can be removed using various vignette correction models. DJI provides a specific set of correction coefficients for the vignette correction model corresponding to the P4M camera:

$$V_{(x,y)} = \frac{1}{(k[5]\times r^6 + k[4]\times r^5 + \cdots + k[0]\times r + 1.0)} \quad (1)$$

where:

$$r = \sqrt{(x - CenterX)^2 + (y - CenterY)^2} \quad (2)$$

CenterX and *CenterY* correspond to the center pixel of the vignette and can be found as tags appended to each image. Vignetting coefficients are provided as image metadata and were extracted using ExifTool.

3.4.3. Radiance Calculation

After we applied vignette and dark current corrections, we converted DN to radiance. The radiance calculation converts DN values to absolute spectral radiance, a physical value with units of W/m^2/sr/nm. This process uses the sensor gain and exposure settings from the image metadata.

To compute the spectral radiance (L) for any image pixel (x, y), the model follows:

$$L = V(x,y).\frac{a_1}{g}.\frac{p - p_{BL}}{t_e + a_2 y - a_3 t_e y} \quad (3)$$

where:

L is the spectral radiance in W/m^2/sr/nm

V(x, y) is the vignette polynomial function for pixel location (x, y) from Equation 1

x, y are the image pixel column and row number, respectively

p is the normalized raw pixel value (DN) normalized following the camera manufacturer specifications (usually includes some level of scaling)

p_{BL} is the normalized dark current value (found in the image metadata)

a_1, a_2, a_3 are the radiometric calibration coefficients

t_e is the image exposure time (found in the image metadata)

g is the sensor gain setting (found in the image metadata)

3.4.4. Surface Reflectance Calculation

We isolated a homogeneous patch of pixels (in units of radiance from Section 3.4.3) from the selected sub-panel in the radiometric calibration images (MAPR or GRP8) using a bounding box. The selected pixels were averaged into a single radiance value (avg (L_i)). The reflectance values (provided by the manufacturer) for the sub-panel were averaged over the full P4M band width (see Section 3.5.1) to produce the reflectance calibration factor, F_i, following equation 4:

$$F_i = \frac{\rho_i}{avg(L_i)} \tag{4}$$

where:

F_i is the reflectance calibration factor for band i

ρ_i is the average reflectance of the radiometric calibration plate for the i^{th} band (from the radiometric calibration data of the panel provided by the MAPR and GRP8 manufacturers)

$avg\ (L_i)$ is the average value of the radiance for the selected pixels inside the sub-panel for band i as measured by the camera and derived by equation 3 in Section 3.4.3.

All pixels in the radiance image were then multiplied by F_i to produce a surface reflectance image. The conversion process from radiance to surface reflectance was repeated for each MS band and radiometric calibration sub-panel selected in Section 3.2.3, following equation 5:

$$\rho_{i(x,y)} = F_i \times L_{i(x,y)} \tag{5}$$

where:

$\rho_{i(x,y)}$ is the i^{th} band surface reflectance for pixel (x,y) in the image

F_i is the reflectance calibration factor for band i, from equation 4

$L_{i(x,y)}$ is the i^{th} band radiance value for pixel (x,y) in the image

For commercial photogrammetric software options, pixels corresponding to a particular sub-panel are manually outlined (i.e., hand-drawn box) or automatically located in the case of reflectance panels containing an identifier (e.g., QR code) supported by the software developer. Reflectance values associated with the sub-panel of interest are entered manually or, in the latter case, automatically ingested. The user provides photogrammetric software with one or more images containing the radiometric calibration panel, masks the image(s) to include only the sub-panel of interest, and radiometrically corrects the MS dataset using reflectance information from one sub-panel at a time.

3.4.5. Lens Distortion Correction

Lens distortion, or fisheye, correction is another key geometric correction process that is unique to the curvature of the lens. The effect of this curvature must be removed from the image, similar to vignette correction. The P4M model uses the *CenterX* and *CenterY* (discussed in Section 3.4.2), a set of de-warping coefficients (*k1, k2, p1, p2, k3*), and intrinsic camera parameters (f_x, f_y, c_x, c_y), all of which are stored in the image (sensor-specific) metadata. This correction process spatially removes the distortion, which is most evident along the edges of the image (Figure 11). The process rearranges all image pixels to their accurate location in the frame following equations 6-11:

$$r = \sqrt{(u^2 + v^2} \tag{6}$$

$$\theta = \arctan(r) \tag{7}$$

$$r_d = D(\theta + k_1 * \theta^3 + k_2 * \theta^5 + k_3 * \theta^7 + k_4 * \theta^9 \tag{8}$$

$$c_d = r_d / r \tag{9}$$

$$u_d = u * c_d \tag{10}$$

$$v_d = v * c_d \tag{11}$$

where:

k_1, k_2, k_3, k_4 are the distortion coefficients

(u_d, v_d) is the coordinate of a point in the distorted image (Figure 11a)

(u, v) is the coordinate of a point in the corrected image (Figure 11b)

$D(\theta)$ defines the mapping from point angle and pixel distance to image center

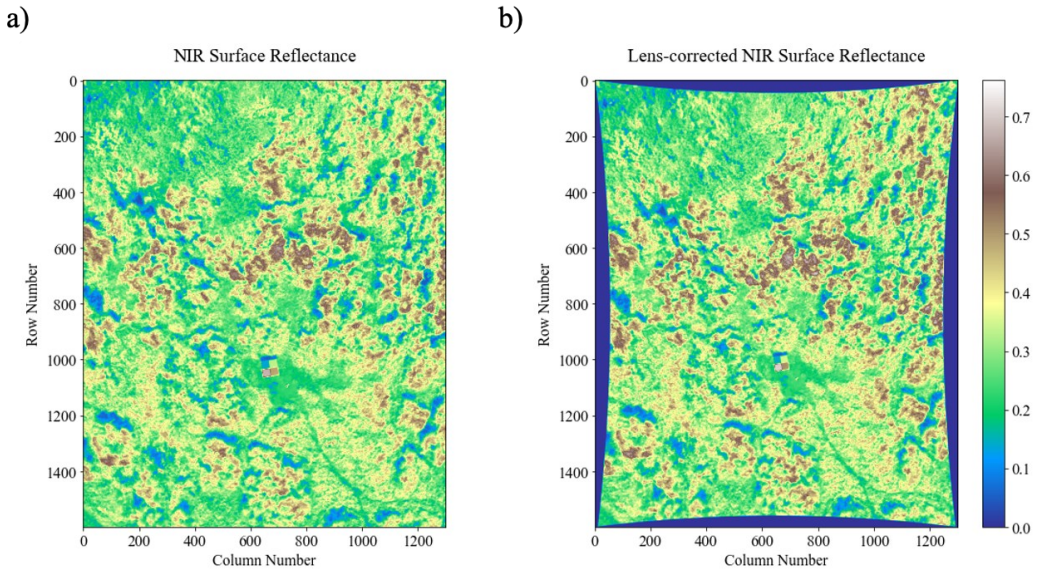

Figure 11. An example of an NIR surface reflectance image (a) prior to and (b) following lens distortion (fisheye) correction. The fisheye correction model compresses the data inward toward the center of the scene.

3.4.6. Band Alignment

As with most MS cameras with individual sensors dedicated to each MS band, displacement between these sensors results in a misalignment of the data. *Relative optical center (ROC) X* and *ROC Y* image metadata describe the physical displacement (in pixels) between each band in the camera. The NIR band is used as the reference for this process, against which all other bands are aligned.

The DJI-provided *ROC* correction values resulted in a poor performance in band alignment. We used an alternative method (also described by DJI) with OpenCV to find tie points in each band followed by a band alignment based on these points. The derived correction values were applied to all images for the particular camera.

3.4.7. Calculation of Vegetation Indices (VIs)

Once aligned, red and NIR MS bands were used to calculate NDVI (Huang et al., 2020; Tucker, 1979) and the two-band enhanced vegetation index (EVI2; (Jiang et al., 2008)) to further demonstrate the performance of these derived surface reflectance data. In addition to being key remote sensing tools for monitoring vegetation, NDVI and EVI2 serve as a quantitative, re-scaled proxy for evaluating sensor performance across the dynamic range of observed vegetative cover. These VIs were also generated from the AOP data for comparison with the UAS data. NDVI and EVI-2 are calculated following equations 12 and 13:

$$NDVI = \frac{(NIR-RED)}{(NIR+RED)} \tag{12}$$

$$EVI2 = 2.5 \times \frac{(NIR-RED)}{(NIR+2.4\times RED+1)} \tag{13}$$

3.5. AOP and UAS Data Harmonization

3.5.1. Spectral Convolution

Spectral convolution in the context of this study is the process whereby the AOP hyperspectral dataset is aggregated across the spectral domain to match the relative spectral response (RSR; sensitivity of an individual MS sensor at each wavelength across its bandwidth) function of each P4M sensor, effectively creating P4M-like blue, green, red, and NIR images at the AOP's native spatial resolution of 1 m/pixel. This requires knowledge of the P4M's RSR corresponding to each sensor in the MS camera. It is common for MS sensors to lack uniformity in sensitivity across the range of wavelengths to which they are sensitive (i.e., a weighted average may more appropriately describe a sensor's sensitivity to a range of wavelengths than does an arithmetic average of the same). DJI did not provide this information, so we digitized the RSR functions published by Lu et al. (2020) for the P4M's green, red, and NIR bands (blue was not reported by the authors) to calculate a weighted average response across the digitized bandwidth for each MS sensor. We also calculated the arithmetic average response over the range of band-specific wavelengths provided by DJI for each MS sensor. The sensitivity of P4M sensors to both MAPR and GRP8 radiometric calibration panels was computed by multiplying each RSR weight (digitized method) by a particular sub-panel's manufacturer-provided reflectance at each wavelength over the RSR range (for a particular MS band), and subsequently divided by the sum of weights digitized across the

same RSR bandwidth. The weighted average reflectance was calculated for each combination of MS band and radiometric calibration panel, separately. Similarly, we calculated the arithmetic average of the P4M sensor response over both MAPR and GRP8 radiometric calibration panels for each MS band, separately. Our assessment of these two approaches did not show a large departure (less than 1.23% in all cases) between the weighted average (digitized RSR) and arithmetic average calculated over both radiometric calibration panels (Figure 12). We opted to perform spectral convolution using the pixelwise arithmetic average of AOP hyperspectral surface reflectance images corresponding to DJI-defined sensitive wavelengths across the bandwidth for each P4M MS sensor (including the blue band).

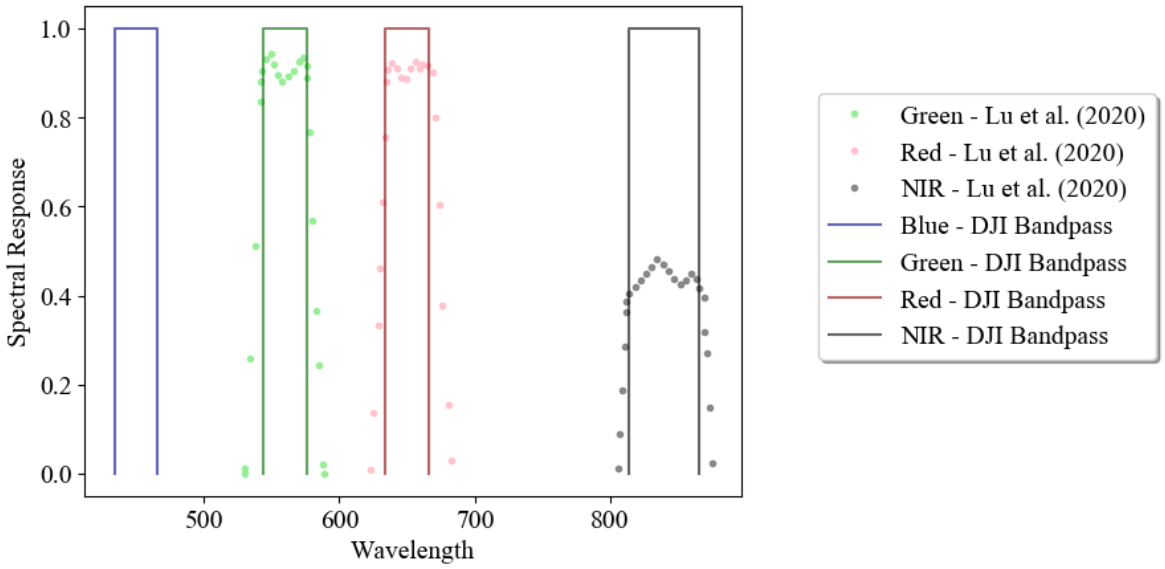

Figure 12. RSR functions (dots) for each of the P4M MS bands, as reported by Lu et al. (2020). The range of wavelengths (solid) to which the P4M is sensitive is provided by DJI for each MS band.

3.5.2. Spatial Convolution

Spatial convolution is the process whereby fully corrected (Section 3.4), native resolution UAS surface reflectance images are degraded (aggregated) to match the nominal AOP spatial resolution (1 m/pixel). We aggregated the UAS images using a Gaussian smoothing model to match the AOP data, which served as the ground truth (validation) dataset. The model generated a 1 m/pixel image from the native (cm-level) UAS data. The method uses a Gaussian distribution to compute a 3-dimensional weighted average matrix kernel which includes the centermost and directly adjacent pixels. The Gaussian blur model is assumed to better account for the influence of pixels directly adjacent to the target pixel relative to other degradation techniques. The kernel used to derive the 1-m pixels is symmetrical in shape and contains the weights ranging between 0 and 1 (Figure 13).

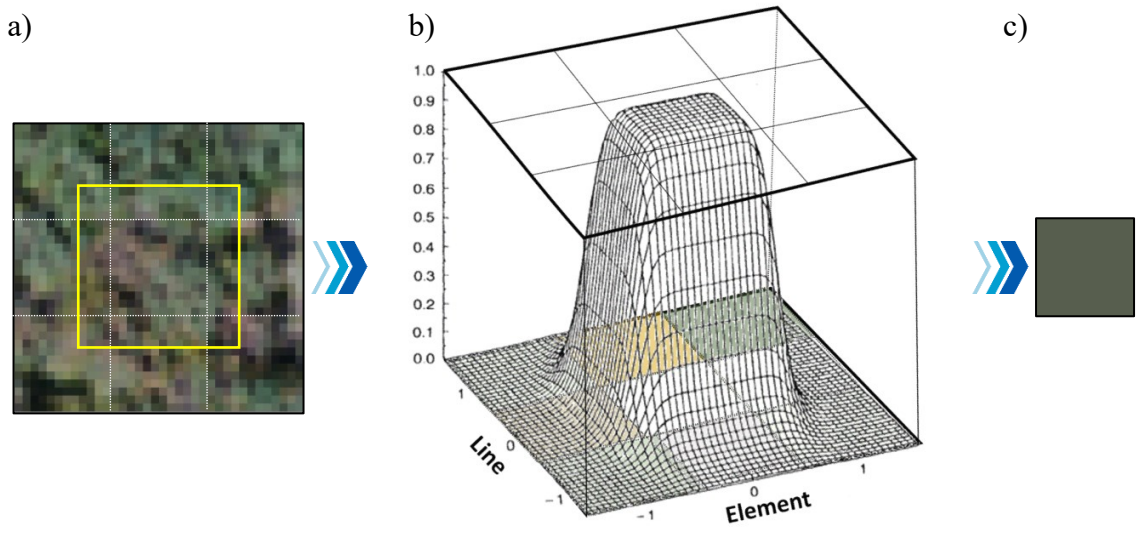

Figure 13. (a) High resolution (cm-level) UAS MS pixels were aggregated using (b) a three-dimensional Gaussian distribution model to derive (c) a UAS dataset with a spatial resolution matching AOP (1 m/pixel).

Additionally, an offset factor enables the user to stretch a particular Gaussian blur model to varying distances within the surrounding pixels. An offset of 0.3 was selected in our case, where approximately one-third of each neighboring pixel contributed to the final, aggregated value. In practice, low-pass filtering techniques like Gaussian smoothing described herein are useful in better approximating the AOP imaging system, which likely reports a superior signal-to-noise ratio (SNR) relative to the P4M.

3.5.3. Image Registration & Pixel Aggregation

Accurate pixelwise comparisons between the UAS and AOP MS bands (for plot and concentric mission types only) required co-registration of the two datasets. This was accomplished by using features identifiable in both datasets to manually "tie" the UAS images to the corresponding features in the AOP imagery. The AOP hyperspectral dataset was too coarse to identify these tie points, so we used the higher resolution AOP RGB dataset (10 cm/pixel). Ten to 15 tie points were visually identified and used to register each UAS image to the corresponding AOP RGB imagery. Congalton and Green (2019) recommend further aggregating to a 3-by-3 pixel to reduce edge effects (between both datasets) and effects of spatial error inherent in each dataset. Aggregating both datasets to 3 m/pixel using the arithmetic average of a 3-by-3 window improved the pixelwise comparison between datasets, while providing adequate pixel counts for statistical analyses.

3.6. Pixelwise Agreement Between UAS and AOP

Root-mean-square error (RMSE) was used to assess agreement between the AOP and UAS datasets:

$$RMSE = \sqrt{\sum_{i=1}^{n} \frac{(\hat{y}_i - y_i)^2}{n}} \quad (14)$$

where $\hat{y}_i$ and y_i are UAS and AOP reflectance values (unitless), respectively. We used RMSE to identify the range of image collection or processing conditions that resulted in the lowest error (i.e., RMSE minimization). For all mission types, a combined spectral reflectance RMSE was produced by adding the sum-of-square-errors (SSE) across all MS bands (blue, green, red, and NIR), dividing by the total number of pixels across all four bands, and calculating the square root of the mean square error term. This consolidated, multi-band Blue-Green-Red-NIR RMSE ($RMSE_{BGRN}$) calculation represents a singular error term for all spectral bands, which reflects how these data are collected in practice (i.e., together on a single camera rig and without concern for individual band performance). NDVI and EVI2 index-specific errors are also reported but provided separately due to differences in scale.

3.6.1. Plot Mission

We examined all combinations of ToD, view angle, flight altitude, and radiometric calibration technique to identify the scenario that resulted in the lowest RMSE between the UAS and AOP data. We note here that the region of common pixels shared by all image acquisitions (i.e., including all altitudes and view angles) did not adequately capture the full range of vegetative cover. The common region of pixels shared across all UAS data was constrained by the lowest flight altitude and the influence of nadir versus off-nadir viewing on image footprint. For this reason, four separate regions-of-interest (ROIs) were designed based on the footprint shared by all image acquisitions for a particular altitude (Figure 14). ROI-40 (based on 40, 60, 80, and 100 m AGL data) was used for all UAS-AOP comparisons because it was the only ROI common to all flight altitudes. ROI-40 ensures all UAS image acquisitions are comparable not only against the AOP MS bands, but also against each other. However, the limited spatial footprint of ROI-40 did not cover an adequate number of bare soil pixels given that the area is mostly vegetated (Figure 15). Conversely, ROI-100 included bare soil but did not permit a direct comparison of error relative to the AOP for UAS data collected at lower flight altitudes.

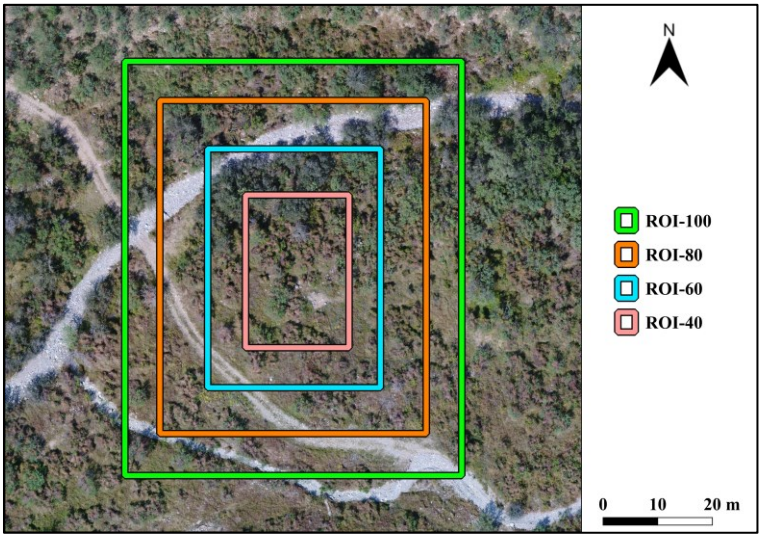

Figure 14. Four ROIs used to analyze global (pixelwise) accuracy between UAS and AOP MS bands. The background 1.4 cm/pixel UAS RGB imagery provides a detailed depiction of the vegetative cover in each ROI.

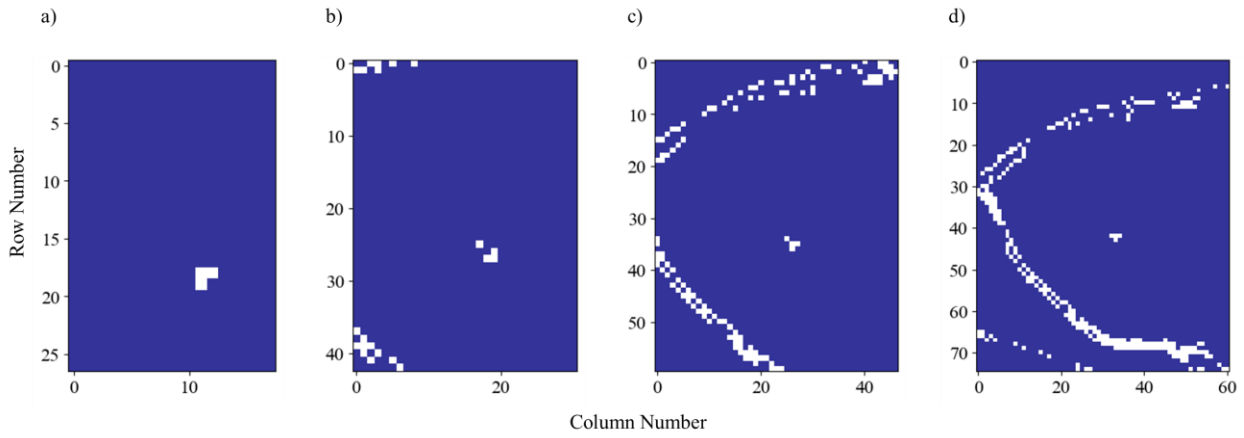

Figure 15. Estimated abundance of soil pixels (white pixels with spatial resolution of 1 m/pixel) in each ROI. The percentage of soil pixels (defined here by NDVI values ranging from 0 to 0.3) present under nadir observation at 12:20 PM local time were reported as follows: (a) ROI-40: 0.6%, (b) ROI-60: 1.6%, (c) ROI-80: 4.2%, (d) ROI-100: 5.4%.

3.6.2. Transect Mission

RMSE minimization was performed on an orthorectified P4M MS dataset produced with Pix4Dmapper (15 images aligned north-south, 75m AGL, georeferenced with 22 GCPs, and radiometrically calibrated with the MAPR 27% panel) collected during the transect mission on September 7, 2021, which captured the full range of vegetative cover (Figure 5a, 8). To further explore any performance differences between UAS and the AOP over variable vegetation densities, the NDVI values were grouped into seven classes: 0 – 0.15, 0.15 – 0.30, 0.30 – 0.45, 0.45 – 0.60, 0.60 – 0.70, 0.70 – 0.80, >0.80. We grouped pixels for UAS and AOP datasets and calculated RMSE for each grouping, separately. Differences in RMSE (compared against the AOP) between these groups would suggest the sensor performance varied with vegetative cover.

3.6.3. Concentric Mission

The number of possible combinations for camera view angle and UAV heading posed an issue for battery performance; therefore, only a subset of camera view angles (10° and 30°) considered during the plot mission were selected to investigate BRDF. Only the MAPR radiometric calibration panel and procedures (BEF, AFT, and NIT) were considered for this analysis. Additionally, the concentric mission utilized the same ROI footprints for comparing UAS and AOP MS bands. At a flight altitude of approximately 70 m AGL, only ROI-40 and ROI-60 contained all pixels shared across each combination of aircraft heading and camera view angle. We restricted the analysis to ROI-40 and ROI-60 to ensure 1:1 correspondence between UAS and AOP datasets. The concentric mission was analyzed similarly to the plot mission, where the data were binned into three separate groups: Blue-Green-Red-NIR (BGRN), NDVI, and EVI2. We evaluated all combinations of UAV heading and camera view angle for the single flight altitude and ToD to identify the lowest RMSE.

3.6.4. Multispectral Data Processing Workflow

We used RMSE minimization across the full image frame at native UAS resolution (aggregation was only required when comparing UAS to the AOP) to compare fully corrected images to partially corrected images, which captured the sensitivity of surface reflectance and value-added VI products to each processing step. The full, recommended processing pipeline was outlined in sections 3.4.1 through 3.4.5 of this report. With this analysis, we are not suggesting that any processing step could be omitted; rather, we are demonstrating the importance of these steps on deriving surface reflectance, and consequently MS data sensitivity to each processing step.

3.6.5. Geolocation Accuracy

We explored the effect of GCP density and distribution on spatial error propagation by calculating both horizontal ($RMSE_X$ and $RMSE_Y$) and vertical ($RMSE_Z$) error of the orthorectified UAS RGB and MS single-grid mission datasets (Section 3.3) using five different ground control configurations: 3, 4, 5, 12, and 22 GCPs. P4M MS data with RTK positional correction and DJI Phantom 4 Pro (P4P) data without RTK correction were collected over the general location of the transect region with approximately 70% forward and 70% side overlap on September 3 and September 29, 2021, respectively. A total of 23 ICs visible across both P4M and P4P datasets were included in RMSE calculations. We also tested the baseline global accuracy potential of the global positioning equipment internal to both the P4P platform and the D-RTK 2 base station (which supported data collection by the P4M platform) by generating orthomosaic maps without using any GCPs, with subsequent error analysis using all ICs.

4. Results and Discussion

4.1. Plot Mission

Table 1 presents the best-performing combination of flight time, view angle, radiometric calibration procedure, and flight altitude, as determined by minimized RMSE for each ROI. Optimal ToD for MS data collection is generally considered to be around solar noon when shadows are minimized and solar elevation angle is at a maximum (Assmann et al., 2019). We note here the association between the AOP's flyover at ~10:30 AM local time and our earliest mission (at approximately 10:35 AM local time) resulted in the lowest RMSE across all ROIs for both BGRN and EVI2. Further, the 100 m AGL flight altitude provided the lowest RMSE across all ROIs for BGRN, NDVI, and EVI2, which could be explained by 1) higher altitudes more closely approximate the conditions of data collected by the AOP and 2) increasing flight altitude tends to improve the SNR and aggregates the finer reflectance of the complex canopy (Assmann et al., 2019) but at the cost of degrading spatial resolution. $RMSE_{NDVI}$ was also minimized for ROI-80 and ROI-100 at 10:35 AM and 100 m AGL; however, this combination of flight time and altitude did not minimize $RMSE_{NDVI}$ for ROI-40 and ROI-60, which also considered lower altitude datasets.

ROI-40 had the lowest $RMSE_{NDVI}$ but differed the greatest in optimal acquisition time and view angle (i.e., 2:15 PM local time and -20°, respectively) when compared to optimized BGRN and EVI2. This may have been a spurious result since the second lowest $RMSE_{NDVI}$ for ROI-40 had an acquisition time of 10:35 AM local time, 0° view angle, radiometric calibration using MAPR 27%

(NIT), and a flight altitude of 100 m AGL. The highest altitude we considered (100 m AGL) resulted in the lowest RMSE in all cases, irrespective of the ROI, ToD, view angle, and radiometric calibration procedure. Based on the UAS data collection parameters and radiometric calibration procedures considered, we observed that a flight altitude of 100 m AGL, 10:35 AM collection time, small view angle (0° to 10°, irrespective of aircraft heading), and NIT radiometric calibration procedure minimized RMSE in most cases (Table 1). 21% and 27% radiometric calibration sub-panels performed similarly well, likely due to their similar reflectance properties.

Figures 16, 17, and 18 depict RMSE for BGRN, NDVI, and EVI2 with respect to time of data collection (subset depicted: 100 m AGL, 0° view angle, and MAPR 27% (NIT) for ROI-40 through ROI-100), view angle (subset depicted: 100 m AGL, 10:35 AM, and MAPR 27% (NIT) for ROI-40 through ROI-100), and flight altitude (subset depicted: 0° view angle, 10:35 AM, and MAPR 27% (NIT) for ROI-40 through ROI-100), respectively. Figure 16 demonstrates the bias of our UAS data toward the AOP overpass time of ~10:30 AM, irrespective of ROI. Figure 17 suggests a potential dependency between view angle and ROI, with RMSE minimized at 10° (W) or 0° (E) heading for ROI-40 and ROI-60, which drifted toward a 10° (E) heading for ROI-80 and ROI-100, possibly due to the change in landcover composition visible at different ROIs. Figure 18 clearly highlights improvements in RMSE for BGRN, NDVI, and EVI2 datasets with increasing flight altitude. Figure 19 illustrates how flight altitude covaries with view angle across all plot mission ROIs using the MAPR 27% (NIT) radiometrically calibrated MS data from 10:35 AM, suggesting a high relative impact of view angle with respect to flight altitude.

RMSE generally increased as ROI footprint increased for BGRN, NDVI, and EVI2. The differences in error across ROIs are likely the result of different vegetative cover, with increasing proportions of soil pixels between ROI-40 and ROI-100, or a slight misalignment between UAS and AOP datasets. Performance across a wide range of vegetative cover is discussed further in Section 4.2.

Table 1. Best Performing UAS MS Data Based on ToD, View Angle, Radiometric Calibration, and Flight Altitude.

Image(s)	ROI	Time[1]	View Angle	Calibration Procedure	Altitude (m)	RMSE
BGRN	40	10:35 AM	0° (E)	MAPR 27% (NIT)	100	0.0119
	60	10:35 AM	0° (E)	MAPR 27% (NIT)	100	0.0131
	80	10:35 AM	10° (E)	MAPR 21% (NIT)	100	0.0154
	100	10:35 AM	10° (E)	MAPR 21% (NIT)	100	0.0171
NDVI	40	2:15 PM	20° (W)	GRP8 56% (NIT) GRP8 36% (NIT)	100	0.0147
	60	11:10 AM	0° (E)	MAPR 27% (AFT)	100	0.0187
	80	10:35 AM	10° (W)	MAPR 27% (AFT)	100	0.0299
	100	10:35 AM	10° (E)	MAPR 27% (NIT)	100	0.0338
EVI2	40	10:35 AM	10° (W)	MAPR 27% (NIT)	100	0.0280
	60	10:35 AM	10° (E)	MAPR 21% (NIT)	100	0.0301
	80	10:35 AM	10° (E)	MAPR 21% (NIT)	100	0.0364
	100	10:35 AM	10° (E)	MAPR 21% (NIT)	100	0.0395

[1] The flight time has been standardized to a single value and represented using a 12-hour (HH:MM) format for each plot mission, as determined by the mission's median image time stamp rounded to the nearest 5-minute step.

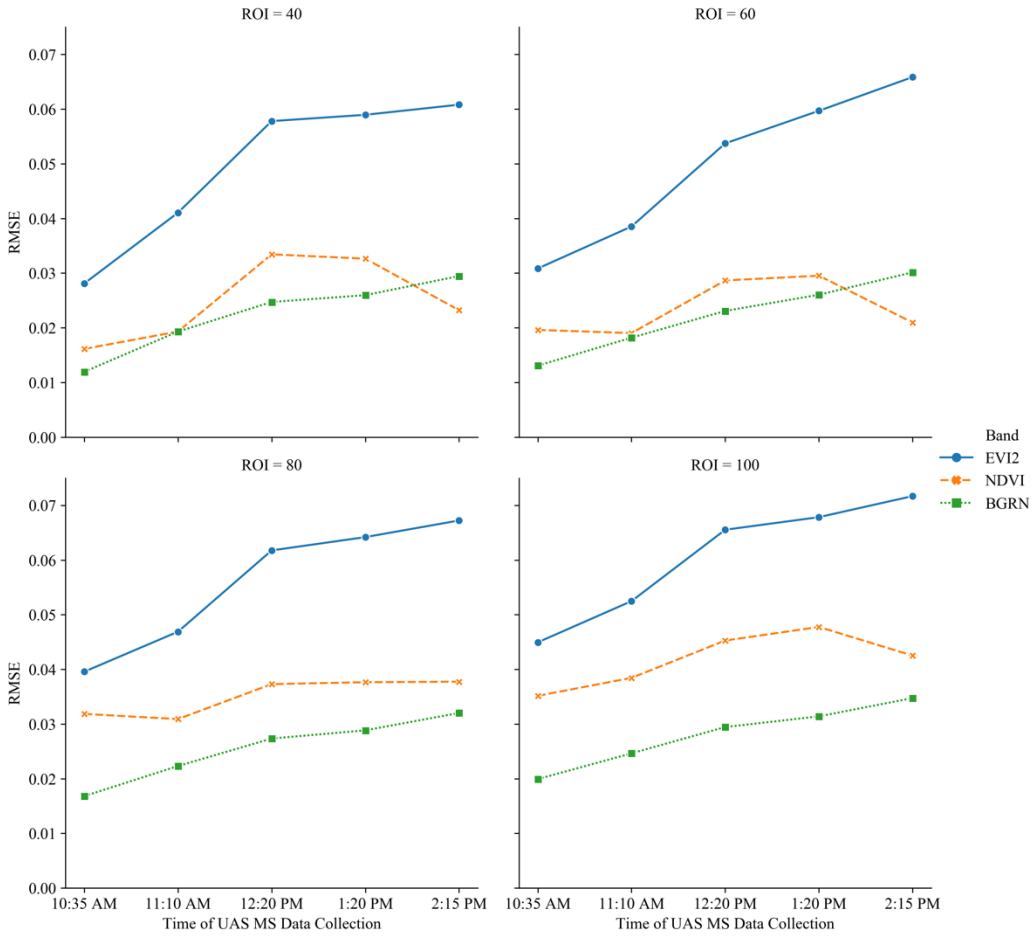

Figure 16. MS data collection timing (with respect to the ~10:30 AM AOP overpass) versus RMSE for BGRN, NDVI, and EVI2 at ROI-40, ROI-60, ROI-80, and ROI-100 (100 m AGL, Nadir, MAPR 27% (NIT)).

.

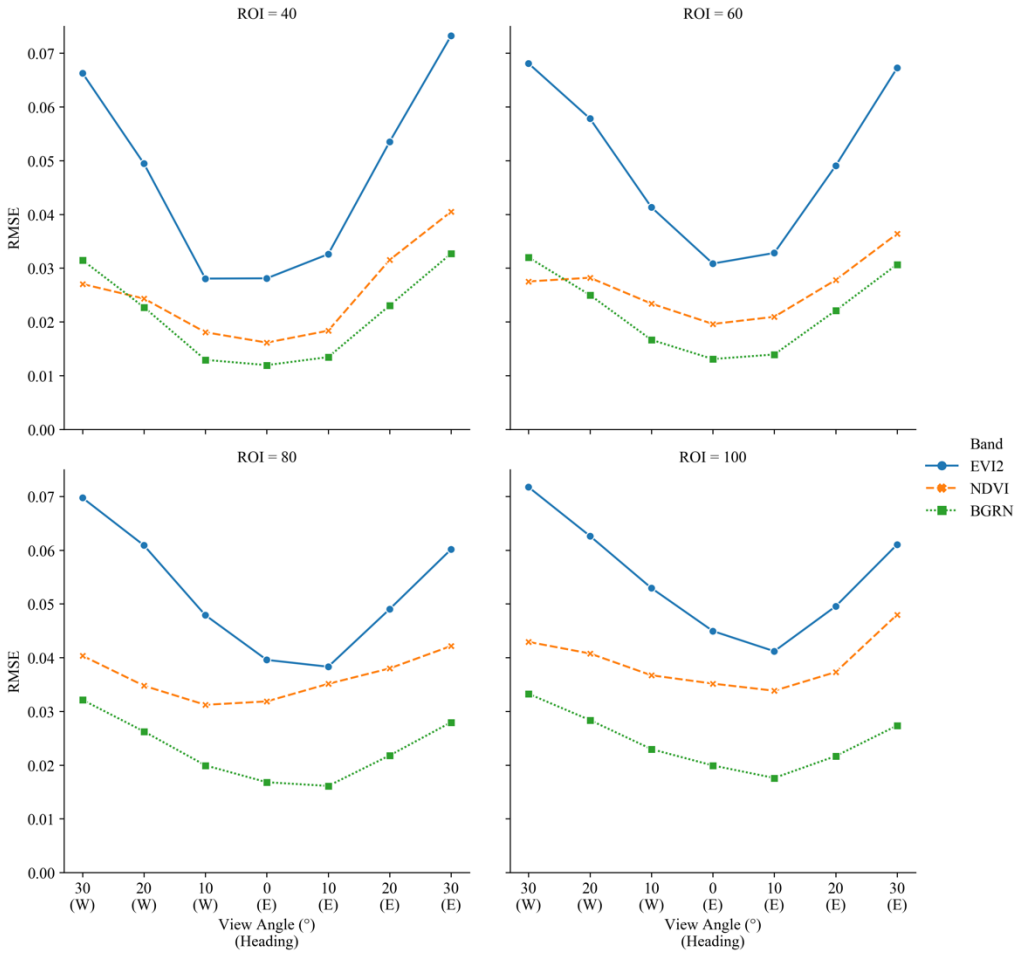

Figure 17. Impacts of view angle on RMSE relative to AOP for BGRN, NDVI, and EVI2 at ROI-40, ROI-60, ROI-80, and ROI-100 (100 m AGL, 10:35 AM, MAPR 27% (NIT)).

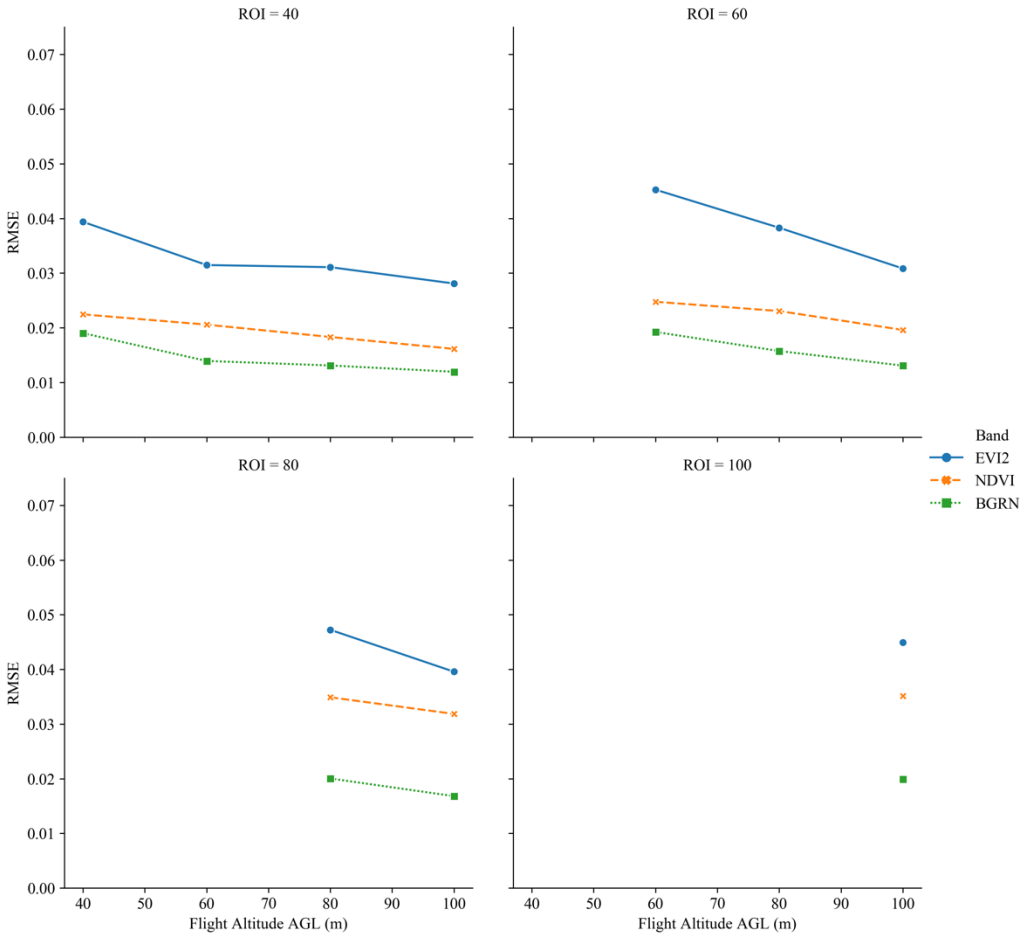

Figure 18. Impacts of flight altitude on RMSE relative to AOP for BGRN, NDVI, and EVI2 at ROI-40, ROI-60, ROI-80, and ROI-100 (Nadir, 10:35 AM, MAPR 27% (NIT)). ROIs support direct comparison of data collected at multiple altitudes, but only for those altitudes greater than or equal to the number appended to the name of each ROI (e.g., for ROI-80, only data collected at 80 and 100 m AGL can be compared).

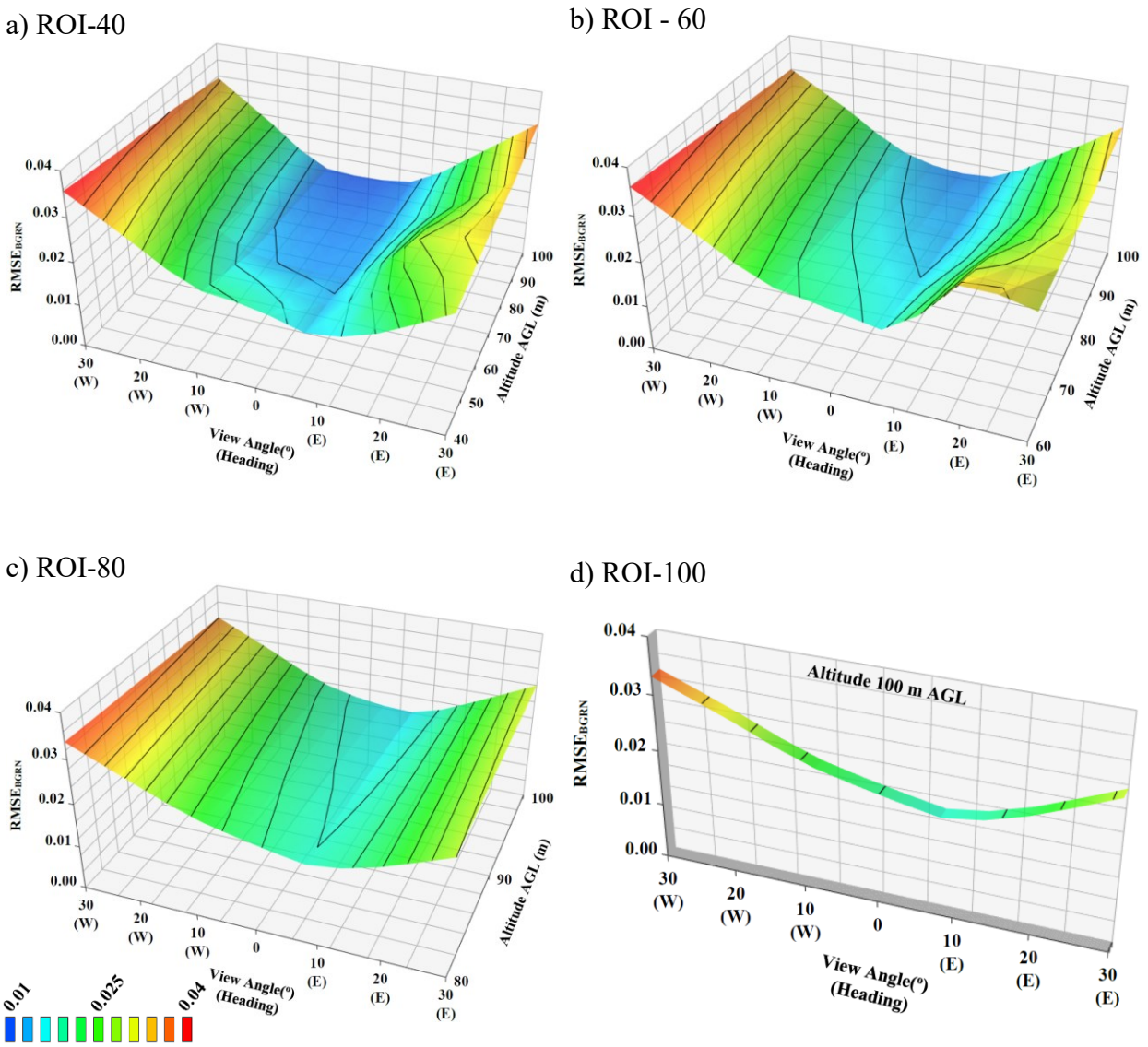

Figure 19. RMSE$_{BGRN}$ between UAS (10:35 AM, MAPR 27% (NIT)) and AOP MS bands for (a) ROI-40, (b) ROI-60, (c) ROI-80 and (d) ROI-100. Increasing the ROI footprint decreases the number of comparative altitudes analyzed in each respective ROI; hence, ROI-100 only shows data for 100 m AGL. Contour lines represent RMSE as a function of flight altitude and viewing geometry.

4.2. Transect Mission

The goal of the transect mission was to investigate the relationship between MS reflectance error and vegetative cover. Figure 20 shows the true-color UAS and AOP imagery derived from red, green, and blue MS bands (aggregated to 3 m/pixel) that were used for the image-to-image comparison (Section 3.5.3). Figure 21 shows where the AOP pixels associated with each NDVI grouping (defined in Section 3.6.2) are located throughout the transect.

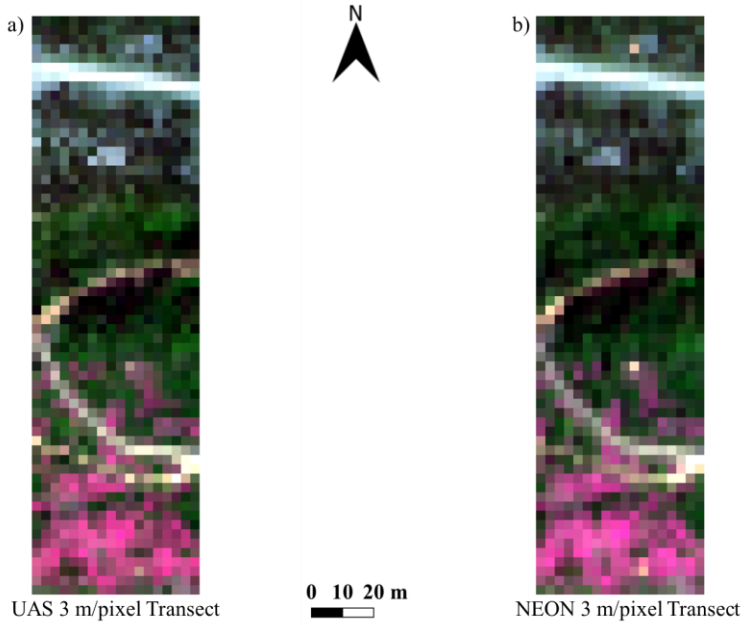

Figure 20. (a) Mosaicked UAS RGB imagery aggregated to 3x3 m along the north-south oriented transect and (b) the corresponding AOP dataset. Light colored (gray or white) pixels correspond to soil, dark green pixels correspond to dense vegetation, and purple-pink pixels are flowers.

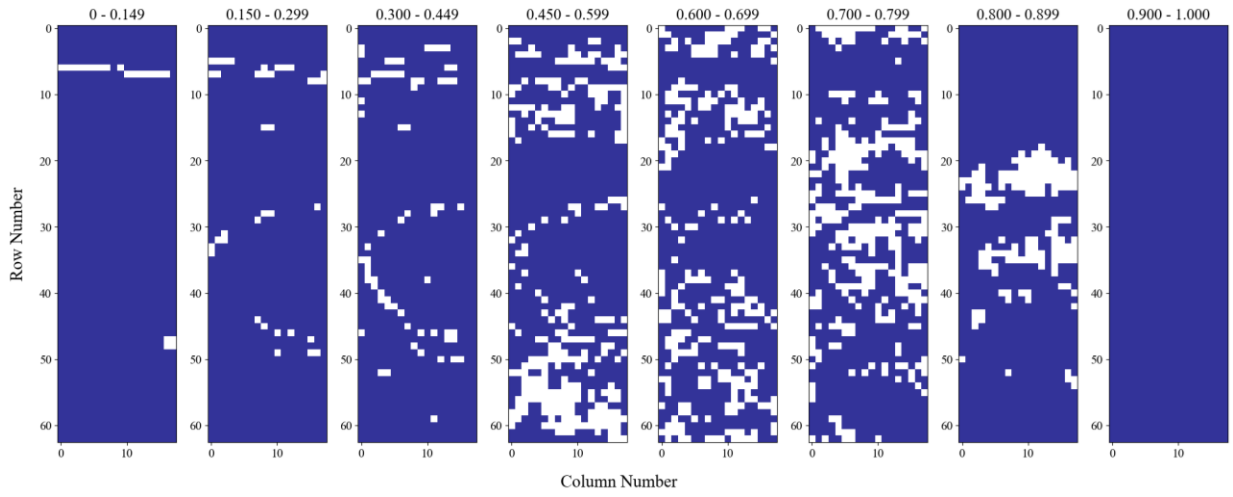

Figure 21. The NDVI grouping scheme presented in Section 3.6.2. Each panel highlights (white pixels) areas with the corresponding NDVI range (defined above each panel) within the transect region.

Figure 22 depicts RMSE for each NDVI class. $RMSE_{Blue}$, $RMSE_{Green}$, and $RMSE_{Red}$ generally decreased with increasing NDVI values, while $RMSE_{NIR}$ generally increased with increasing NDVI. $RMSE_{NDVI}$ and $RMSE_{Red}$ shared similar trends of low RMSE at low and high NDVI, both of which peaked from ~0.3 to 0.45 NDVI. $RMSE_{EVI2}$ generally increased with increased vegetation density (like $RMSE_{NIR}$).

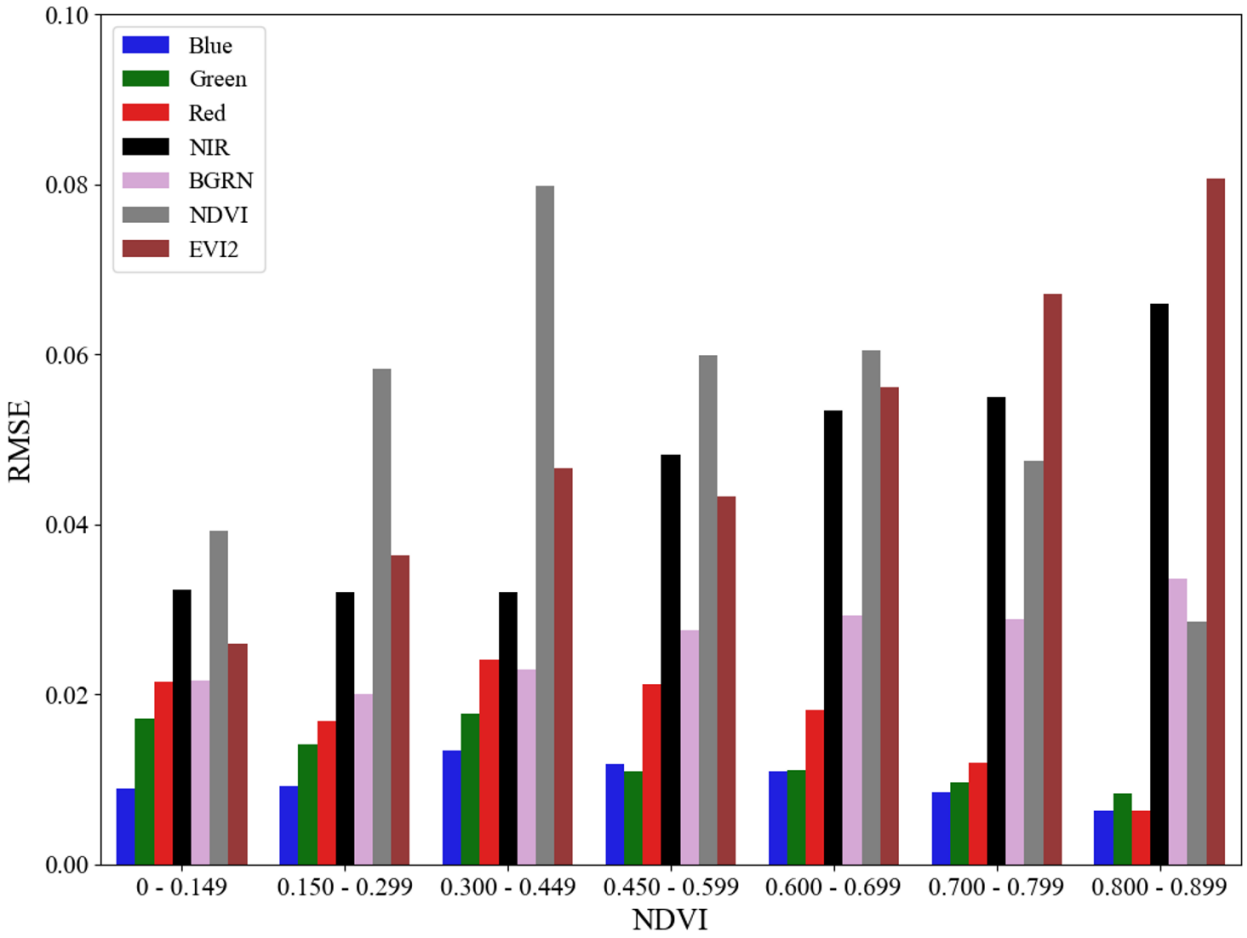

Figure 22. RMSE for individual MS bands, BGRN, NDVI, and EVI2 (by class at 3 m/pixel, as defined by NDVI groupings).

Using the orthorectified transect dataset from September 7, 2021 (described in Section 3.4), Figure 23 shows the impact of calibrating a near-noon MS dataset with radiometric calibration readings of the same panel at multiple times across the day. The outcome is a reading of panel reflectance with increasing departure from the correct reading collected NIT to the actual MS transect mission. The NDVI algorithm appears to minimize the differences in panel reflectance and subsequent impacts to relative accuracy better than the composite BGRN or EVI2. The impacts to relative accuracy are especially noticeable in the composite BGRN and EVI2 datasets beyond approximately ±1 hour of the NIT radiometric calibration reading.

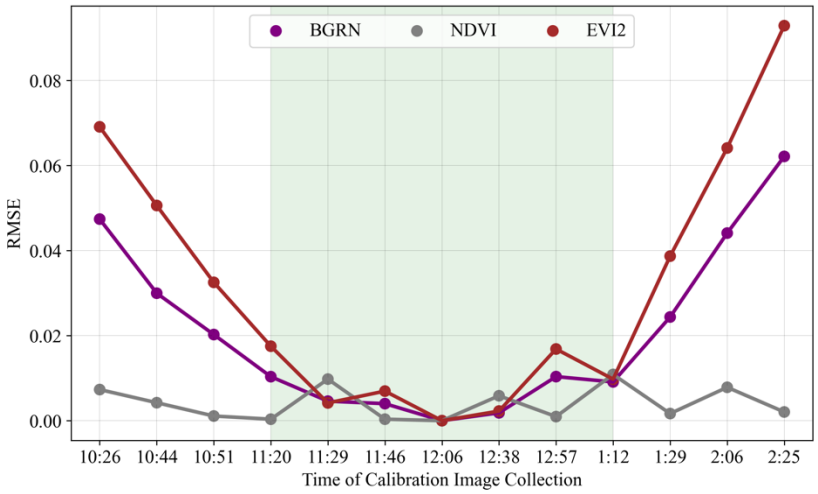

Figure 23. Relative radiometric error of BGRN, NDVI, and EVI2 datasets with respect to the NIT, 12:06 PM calibration image. Calibration data captured within ±1 hour of MS data minimizes error (green region).

4.3. Concentric Mission

BRDF did not have a clear effect on UAS data accuracy, possibly due to the time difference between the UAV and AOP flights (12:45 PM and 10:35 AM local time, respectively). Our findings suggest UAS data accuracy (as measured by RMSE) degrades as one collects data increasingly off-nadir (Table 2; Figure 17, 19); however, this view-angle dependency was confounded by the aircraft heading, which varied by the view angle and ROI (Figure 24). The concentric analysis presented here did not clearly identify a best practice to account for solar-sensor geometry, which was reported by the National Oceanic & Atmospheric Administration (NOAA) Earth System Research Lab (n.d.) as a solar azimuth angle of 193° and an elevation angle of 63° at the time of flight. Canopy complexity may have confounded the concentric mission as well, which is exacerbated in datasets with high spatial resolution.

Table 2. Best Performing UAS Observations Collected during the Concentric Mission: 70 m AGL and 12:45 PM.

Image(s)	ROI	View Angle	Calibration Procedure	Heading	Relative Azimuth	RMSE
BGRN	40	10°	MAPR 27% (AFT)	100°	85°	0.0219
		30°	MAPR 21% (NIT)	60°	45°	0.0227
	60	10°	MAPR 27% (AFT)	100°	85°	0.0205
		30°	MAPR 27% (NIT)	80°	65°	0.0212
NDVI	40	10°	MAPR 21% (AFT)	260°	-115°	0.0216
		30°	MAPR 21% (BEF)	300°	-75°	0.0258
	60	10°	MAPR 21% (AFT)	140°	125°	0.0237
		30°	MAPR 27% (NIT)	100°	85°	0.0289
EVI2	40	10°	MAPR 27% (AFT)	60°	45°	0.0449
		30°	MAPR 21% (NIT)	60°	45°	0.0485
	60	10°	MAPR 27% (AFT)	80°	65°	0.0435
		30°	MAPR 21% (AFT)	60°	45°	0.0452

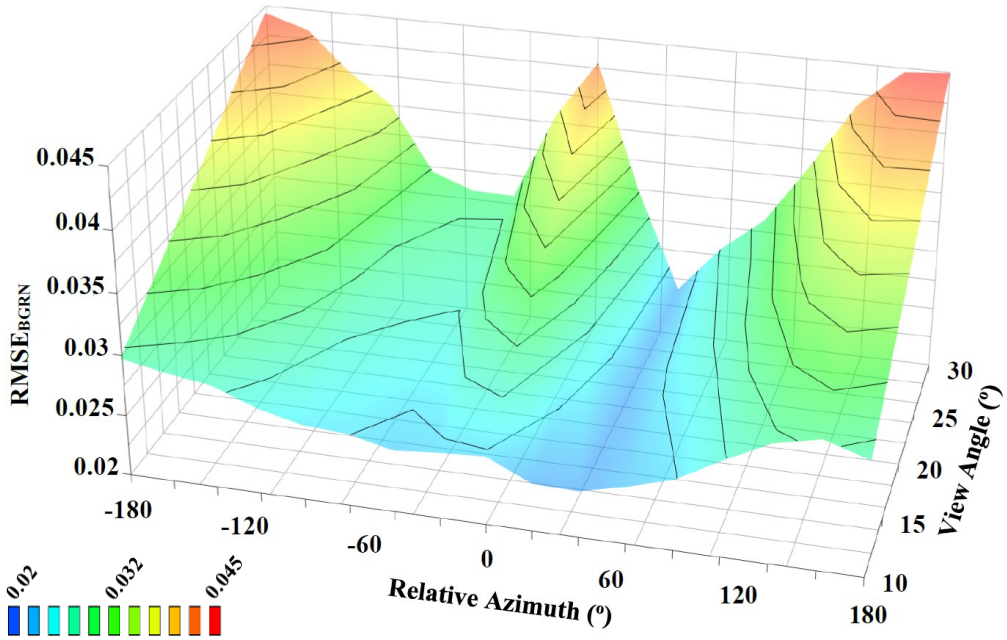

Figure 24. RMSE$_{BGRN}$ between UAS and AOP MS bands for 10° and 30° off-nadir across 360° of UAV heading (12:45 PM, MAPR 27% (NIT), 70 m AGL). Contour lines represent RMSE as a function of camera relative azimuth and viewing geometry.

4.4. Multispectral Data Processing Workflow

The requirements for processing UAS MS data call for a series of precise processing steps (Figure 10) that must be followed to generate accurate and traceable surface reflectance. These steps modify the data with varying degrees from simple (e.g., band alignment) to complex (e.g., conversion of DNs to radiance). We assessed the sensitivity of surface reflectance to these processing steps in case they were applied incorrectly or improperly parameterized. Figure 25 illustrates the impact of each of these steps during the conversion from DN to surface reflectance, especially correcting for lens distortion – a critical step that adjusts the location of each pixel in the scene, without which the data cannot be accurately compared to the AOP or across time.

Figure 26 illustrates the magnitude of impact (on a common scale) when one or more of the image processing steps are omitted. Images in Column A are final products (surface reflectance) resulting from the truncated processing scenarios. Relative to the other, sub-optimal image processing scenarios, impacts are evident in the image variations in color (i.e., data values) as well as changes to the distribution and magnitude of pixel values along the transect plotted in Column B. The differences in performance relative to the corresponding, fully corrected, native resolution UAS image are most easily visualized through difference maps (Column C) and difference histograms (Column D). Difference maps highlight both magnitude and location of impact across the image (land cover dependency), which clearly shows a disproportionate impact of lens distortion correction. This is also apparent in the difference histograms, which show a tight clustering around zero for those scenarios that included correction for lens distortion, while those scenarios omitting the procedure showed generally wider distributions with more exaggerated tails. This confirms the importance of correcting lens distortion, which needs to be implemented accurately to ensure valid spatiotemporal analyses over time.

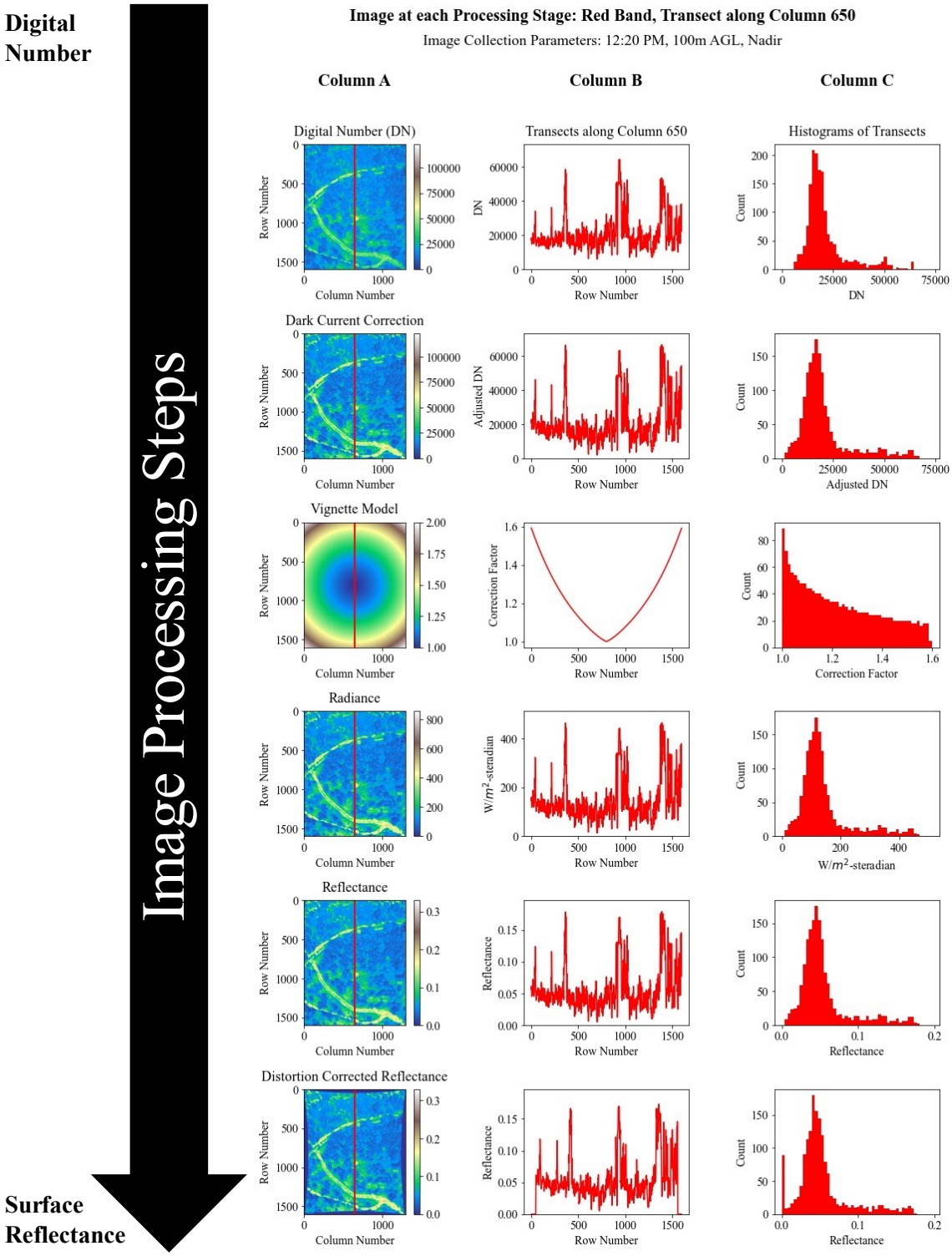

Figure 25. Plots showing the transformation of a UAS image (red band, in this case) as it undergoes various image processing corrections (Column A), changes to a transect (red line) of image pixels (Column B) and changes observed in the data distribution for the same transect of data (Column C).

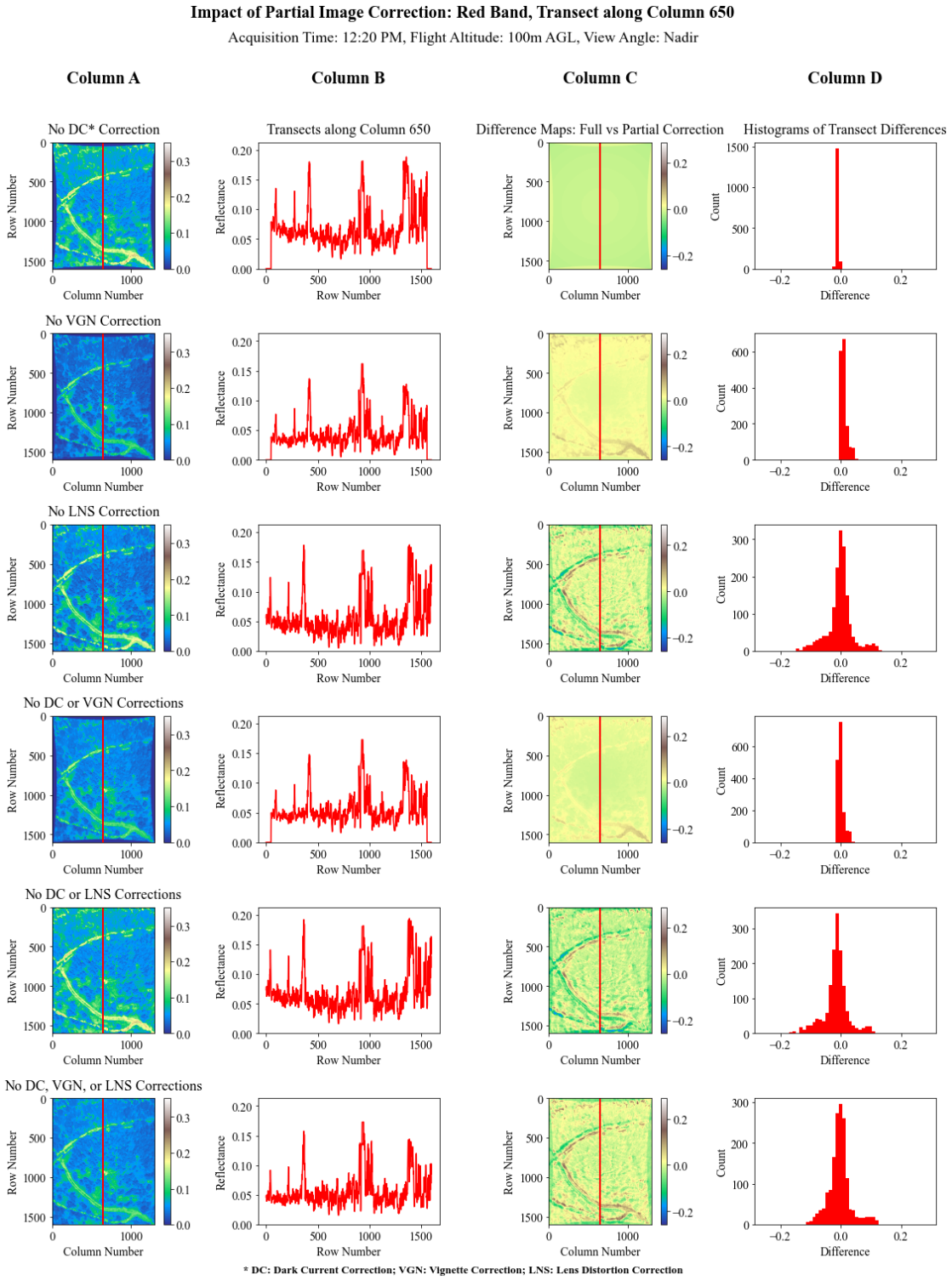

Figure 26. Various scenarios of sub-optimal image correction, wherein one or more image processing steps were neglected. All images depict pixels with units of surface reflectance. Transect data (visible on the images in Column A) illustrates pixelwise differences in the final surface reflectance image depending on the omitted image correction steps.

Figure 27 provides RMSE for the scenarios presented in Figure 26 for individual MS bands, BGRN, NDVI, and EVI2. The differences between the image correction procedures presented in Figure 26 do not suggest that only some procedures should be preserved or prioritized, since these procedures likely interact to confound one another. In practice, all steps should be included in the image processing pipeline unless directed by the MS sensor manufacturer or required by a specific experimental setup. It is worth noting that the NIR band, with a consistently higher RMSE relative to other MS bands, had a disproportionately greater impact on $RMSE_{BGRN}$ for all image processing scenarios considered.

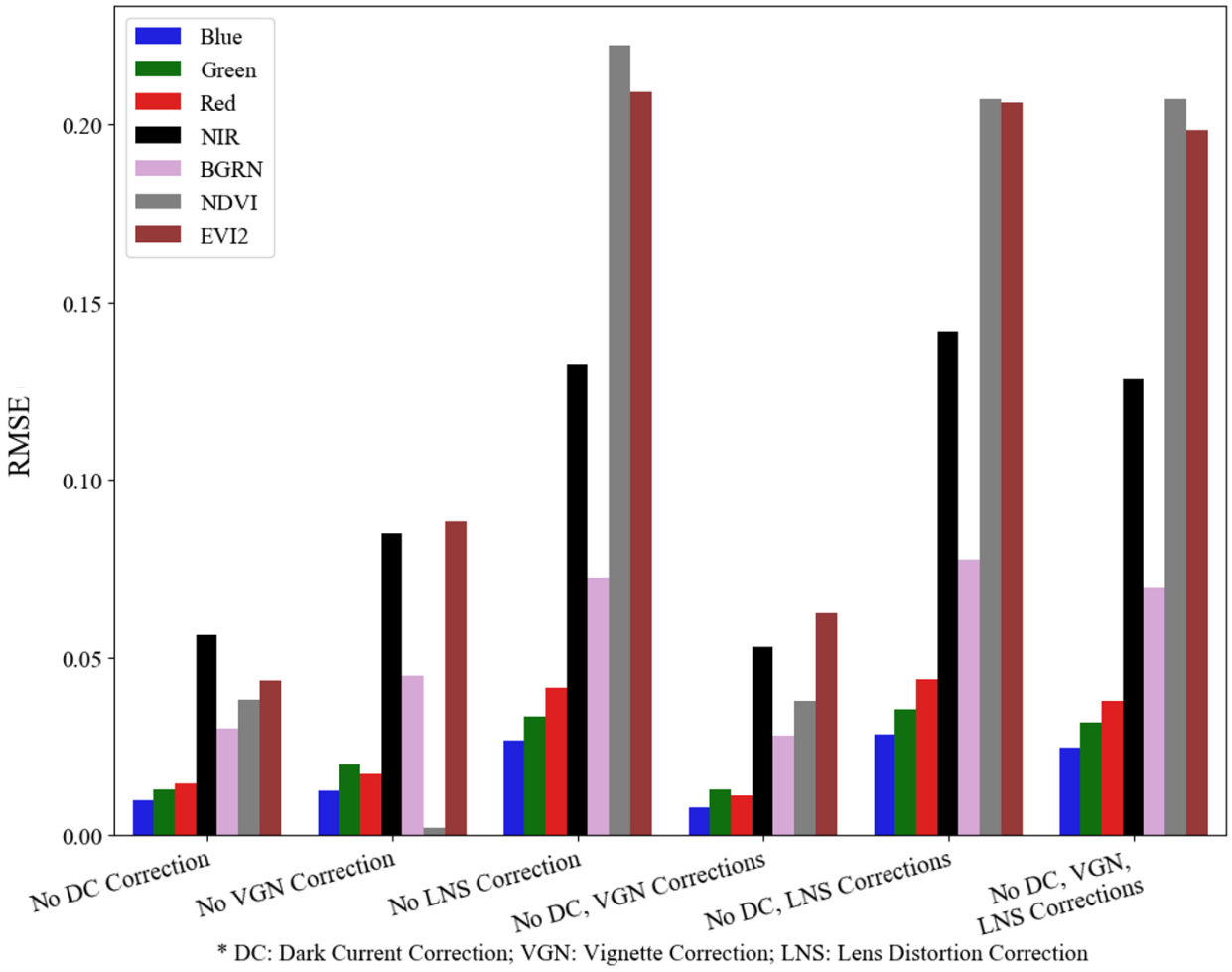

Figure 27. RMSE of individual MS bands, BGRN, NDVI, and EVI2 (relative to the fully-corrected UAS MS image presented in Figure 25) which resulted from truncating the image processing workflow.

4.5. Geolocation Accuracy

Rangel et al. (2018) suggest cm-level accuracy can be achieved by following ASPRS recommendations for GCP density and placement (with the use of survey-grade equipment to record GCP and IC locations). Within a 1-km distance from the D-RTK 2 base station, DJI indicates RTK correction can provide 0.01 m and 0.02 m accuracy in the horizontal and vertical

dimensions, respectively. We investigated the effects of 5 distinct GCP configurations (Figure 28), RTK used in tandem with GCPs, and differences in spatial error between high-resolution, non-survey-grade RGB (0.013 m/pixel) and slightly coarser, survey-grade (RTK) MS imagery (0.027 m/pixel).

Table 3. GCP Configuration Errors with MS (RTK) and RGB (non-RTK) Single-grid, Orthorectified Datasets.

UAS Dataset	Error (m)	0 GCPs	3 GCPs	4 GCPs	5 GCPs	12 GCPs	22 GCPs	Δ 0 vs 4 GCPs	Δ 4 vs 22 GCPs
P4M MS with RTK (Sept 3)	$RMSE_X$	0.330	0.043	0.043	0.043	0.042	0.040	0.288	0.003
	$RMSE_Y$	0.594	0.057	0.052	0.051	0.051	0.052	0.542	0.001
	$RMSE_Z$	3.587	0.080	0.100	0.087	0.074	0.072	3.487	0.028
P4P RGB without RTK (Sept 29)	$RMSE_X$	1.560	0.042	0.039	0.041	0.036	0.036	1.521	0.003
	$RMSE_Y$	1.330	0.044	0.039	0.042	0.039	0.039	1.291	0.000
	$RMSE_Z$	52.988	0.347	0.108	0.093	0.083	0.075	52.880	0.034

Table 3 presents the RMSE calculated from 23 ICs visible in both MS and RGB single-grid mission datasets for each projected spatial dimension (X, Y, Z). Figure 28 depicts these error measurements graphically, excluding the scenario which did not incorporate GCPs in the orthorectification process. Without the use of GCPs to finetune the positioning of the imagery, $RMSE_X$, $RMSE_Y$, and $RMSE_Z$ were substantially lower for the RTK-enabled MS dataset than the RGB imagery, despite differences in spatial resolution (Table 3). Both RGB and MS horizontal and vertical accuracies improved considerably with the inclusion of 4 GCPs. Only a marginal improvement in horizontal accuracy was observed going from 4 to 22 GCPs, with a RMSE difference of 0.000 m to 0.003 m across datasets. We conclude that horizontal accuracy exhibited marginal differences beyond the use of 4 GCPs, including for applications where RTK was used. For the RGB dataset lacking RTK correction, vertical accuracy consistently improved as more GCPs were added. Depending on the application and required vertical accuracy, alternative GCP configurations (i.e., GCP count and distribution density) may be required. While baseline (i.e., without the use of GCPs) positioning capabilities internal to the P4P aircraft (GPS) and RTK-supported P4M differed considerably, neither device provided standalone (i.e., without the use of surveyed GCPs) horizontal or vertical accuracies necessary for modern UAS mapping applications. While 3 GCPs resulted in acceptable vertical accuracy ($RMSE_Z$ = 0.080 m) for the MS data, vertical accuracy was considerably lower for the RGB dataset using the same GCP configuration ($RMSE_Z$ = 0.347 m). Finally, in several cases we observed horizontal accuracies that were higher for the RGB datasets when compared to the MS datasets. We suspect this discrepancy stems from the higher spatial resolution of the RGB dataset, which although the final product did not benefit from RTK, the resulting dataset did benefit from higher spatial resolution in terms of accurately selecting the centroid of each GCP.

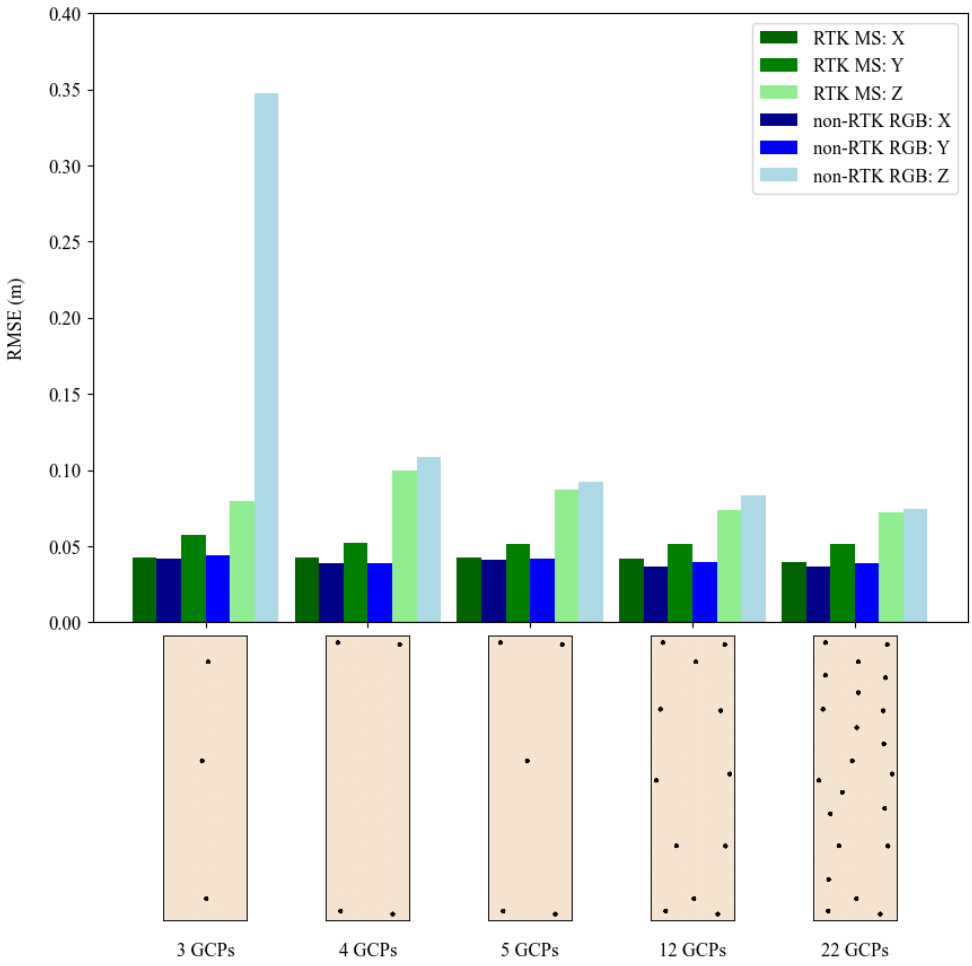

Figure 28. Scenarios used to test the effect of GCP count and distribution on horizontal and vertical accuracy of UAS MS and RGB imagery. Bar plot depicts measures of RMSE (m) for the corresponding GCP configurations (black dots).

5. Data Acquisition and Processing Guidelines

5.1. MS Data Collection

- *Flight Time*: A collection time of 10:30 AM resulted in the most accurate data relative to the AOP; however, this observation was confounded by the AOP's acquisition time. Assmann et al. (2018) recommend collecting MS data as close to solar noon as possible, with a maximum departure from this best practice no greater than ±2-3 hours.
- *Flight Altitude*: Our findings indicate higher altitudes are preferable. 100 m AGL (approaching the FAA limit) performed best in the current study.
    - For MS observation, the advantage of high resolution data is offset by excessive noise caused by canopy structure, shadows, and the exposure of the more complex canopy side profile.
- *View Angle*: ≤10°. Nadir viewing is ideal, as it standardizes the top-of-canopy view.

- *Radiometric Calibration Procedure*: Radiometric calibration should utilize the radiometric calibration data collected nearest in time to the MS data it is intended to correct.
    - Missions longer than those explored here (i.e., approximately 20-30 minutes) should consider more frequent calibration plate readings. Based on our observations (Figure 23), we recommend radiometric calibration images be collected within ±1 hour of collecting the MS data requiring calibration.
    - An alternative approach (not evaluated here) would be to use a second MS camera to continuously image the calibration panel during the entire flight. The resulting panel readings would then be used to time-match and calibrate the MS images.
    - Radiometric calibration panels should be pre-calibrated by the panel manufacturer, delivered with supporting documentation (e.g., spectroradiometer measurements), and utilized in a way that preserves the integrity of the panel specifications (e.g., protected from prolonged exposure to the elements).
    - All manufacturer guidance regarding maintenance and routine re-calibration should be followed. Consult the National Institute of Standards and Technology for guidance on working with traceable calibration standards (Yoon and Kacker, 2015).
- *Dynamic Range:* The recommended MS data collection procedures should not change based on observed vegetative cover (our proxy for sensor dynamic range). However, practitioners can expect larger error over less vegetated areas in the visible bands and NDVI, and a larger error in the NIR and EVI2 over vegetated areas. This is mostly predictable, as NDVI tends to respond more to the red band and EVI2 responds more to the NIR band.
- *Ground Control:* Over our relatively small study area (approximately 200 m x 50 m), including >4 GCPs only marginally improved horizontal accuracy; however, additional GCPs should be used to achieve higher vertical accuracies if terrain models will be derived from the data.

5.2. MS Data Processing

- *Dark Current Correction*: Consult manufacturer and image metadata for offset values. If metadata are missing or unavailable, a simple closed shutter image (or collected in an entirely dark room) should generate this required information.
- *Vignette Correction*: Consult manufacturer and image metadata for vignette model parameters. Most cameras will provide the necessary vignette parameters, but there are also commercial and open-source tools (like OpenCV) that can be used.
- *Lens Distortion Correction*: Consult manufacturer and image metadata for lens distortion correction parameters. If lens distortion correction parameters are not provided, identify and implement the standard lens distortion correction model that most closely matches the lens characteristics of your MS camera.
- *Image alignment*: Consult manufacturer and image metadata for band-to-band alignment parameters. OpenCV and other open-source tools can also be used to identify tie-points between bands. However, we recommend that the suggested (x,y) offsets be confirmed before implementation.

Acknowledgements

The authors of this report want to thank Brian Zimmerman, DOE LM project manager, for his valuable contributions to this project, including input and feedback on this report. Special thanks to Eduardo Jimenez Hernandez, Ph.D. student, who helped with field work.

This work was supported by the DOE LM Applied Studies and Technology (AS&T) Program under grant #DE-LM0000479 awarded to the University of Arizona, Biosystems Engineering Department, VIP Lab (Dr. Kamel Didan, PI).

6. References

Assmann, J.J., Kerby, J.T., Cunliffe, A.M., Myers-Smith, I.H., 2019. Vegetation monitoring using multispectral sensors — best practices and lessons learned from high latitudes. J. Unmanned Veh. Sys. 7, 54–75. https://doi.org/10.1139/juvs-2018-0018

Congalton, R.G., Green, K., 2019. Thematic Map Accuracy Assessment Considerations, in: Assessing the Accuracy of Remotely Sensed Data. CRC Press, pp. 77–106. https://doi.org/10.1201/9780429052729-6

Di Girolamo, L., 2003. Generalizing the definition of the bi-directional reflectance distribution function. Remote Sensing of Environment 88, 479–482. https://doi.org/10.1016/j.rse.2003.07.004

DJI, 2020. P4 Multispectral Image Processing Guide (No. v1.0).

Gallery, W., 2022. NEON Algorithm Theoretical Basis Document (ATBD): Spectrometer Mosaic.

Harvey Phil. 2023. ExifTool: Read, Write and Edit Meta Information. https://www.exiftool.org/. (Last accessed 02/26/2023).

Huang, S., Tang, L., Hupy, J.P., Wang, Y., Shao, G., 2020. A commentary review on the use of normalized difference vegetation index (NDVI) in the era of popular remote sensing. J. For. Res. https://doi.org/10.1007/s11676-020-01155-1

Jiang, Z., Huete, A., Didan, K., Miura, T., 2008. Development of a two-band enhanced vegetation index without a blue band. Remote Sensing of Environment 112, 3833–3845. https://doi.org/10.1016/j.rse.2008.06.006

Lu, H., Fan, T., Ghimire, P., Deng, L., 2020. Experimental Evaluation and Consistency Comparison of UAV Multispectral Minisensors. Remote Sensing 12, 2542. https://doi.org/10.3390/rs12162542

National Oceanic & Atmospheric Administration (NOAA) Earth System Research Lab (ESRL), n.d. Solar Position Calculator [WWW Document]. URL https://gml.noaa.gov/grad/solcalc/azel.html (accessed 9.27.22).

Rangel, J.M.G., Gonçalves, G.R., Pérez, J.A., 2018. The impact of number and spatial distribution of GCPs on the positional accuracy of geospatial products derived from low-cost UASs. International Journal of Remote Sensing 19.

SPH Engineering. 2023. UgCS: Drone Flight Planning and Control Software. www.ugcs.com. (Last accessed 02/26/2023

Tucker, C.J., 1979. Red and photographic infrared linear combinations for monitoring vegetation. Remote Sensing of Environment 8, 127–150. https://doi.org/10.1016/0034-4257(79)90013-0

Wang, C., 2021. At-Sensor Radiometric Correction of a Multispectral Camera (RedEdge) for sUAS Vegetation Mapping. Sensors 21, 8224. https://doi.org/10.3390/s21248224

Yoon, H.W., Kacker, R.N., 2015. Guidelines for Radiometric Calibration of Electro-Optical Instruments for Remote Sensing (No. NIST HB 157). National Institute of Standards and Technology. https://doi.org/10.6028/NIST.HB.157